

## **Reply to reviewer #1.**

*We thank the reviewer for the very positive and helpful comments. Below, we provide point-by-point replies to the comments. Our replies are given in blue and the original comments from the reviewers are in black.*

Dear editor, I read the manuscript from Zhong and co-authors with great interest. Their manuscript deals with several open questions in the field of elastic thermobarometry and the results provided by the authors can be very useful to the community. Apart from the lengthy, but necessary, theoretical derivations provided by the authors, this manuscript has significant results when it comes to the application of Raman elastic thermobarometry. In addition, I find their new results on the application of the “volumetrically averaged stress” and the “irregularly faceted inclusions” very interesting and of exceptional quality. Finally, it is very rare to find such studies where the authors have tested their analytical work so extensively.

### **General Comments**

My major point of criticism concerns the detailed and clear description of the steps involved in the procedure for the calculation of the eigenstrain. I have written in detail my main points below but they concern the clarity of the presentation and not the actual methodology (which is actually based on well-established theories). I believe that this part may be difficult to the petrological community and some things which are considered basic in other fields need to be explained in more detail here.

### **Specific Comments**

l. 27-28: Please be more specific that you refer to cases with garnet hosts.

*Revised as suggested.*

l. 36-37: Somewhere here is implied that you need an elastic model to recover the entrapment conditions. The reason I make this distinction is because one may confuse the elastic model that can be done to convert strains (from vibrational mode shifts) to pressure, with the elastic model that is performed to calculate entrapment conditions from residual P. Please be more specific.

*Revised as suggested.*

l. 40: Zhang's model allows non-infinite host, it is more general.

*Corrected. We removed the word "infinite". The existing model considers an isotropic inclusion in isotropic host.*

l. 50: "no numerical software or programming is required". Theoretically, one could do things by hand (even FEM), in addition, plotting the analytical solution may be more efficient by a software such as Matlab. I would rephrase as "...is that the solution is exact and can be obtained rapidly..."

*Revised as suggested.*

l. 51-52 Please add a relevant reference that relates MC with Uncertainty propagation.

*Reference about MC has been added.*

l. 69: "The MATLAB code", which MATLAB code, of the analytical solution, of the FE? Please be more specific.

*We have revised this sentence to clarify the point. We only present the MATLAB codes for calculating the 1) Eshelby tensor, 2) lattice strain and 3) effective ellipsoidal shape. No FE code is given. This is made clear now.*

l. 118-120: I do not quite follow what you mean here ("The thermal effects..."). Could you please develop a bit more?

*We have revised this sentence. We realized that thermal effect can be confusing as it is often related to volume change, but we are here referring to the T dependence of the stiffness tensor, which has no effect on the final result. This is made clear here now.*

l. 121: I think that this way of formulating may be confusing. My point is that the eigenstress is what it is (as defined in Eq. 2) and any mineral can have it no matter how stiff or soft. However, if I understood your argument correctly, for a very soft inclusion in an infinitely rigid host, its eigenstress will be equal to its actual stress. The reason why I would be so

specific is because the way it's currently expressed it looks that eigenstresses can be defined only for soft minerals in rigid inclusions.

*We see the confusion here. We have revised this sentence. The eigenstress can be understood as the equilibrated stress for an infinitely soft inclusion in an infinitely stiff host. But for practical inclusion and host system, it is just an internal stress that loads the system.*

l. 136, what is the “equivalent eigenstrain”? How it is different from the previous one. Could you be more specific? Please also add that the equivalent eigenstrain is yet unknown and needs to be solved for. I think this part deserves a bit more development so clarify some details that may not be obvious to the reader who is not familiar to the Eshelby solution. In that case I would highlight if the stress balance solved for or if it is satisfied by the solution (i.e. is given). In addition, I would highlight that eigenstrain is needed in order to have “equivalent” loading conditions.

*We have added several new sentences here to clarify the concept of the equivalent eigenstrain and the use of the Eshelby's tensor, which transforms the loaded inclusion eigenstrain into the final strain that is under mechanical equilibrium with the host.*

l. 143, as before: please mention how the Eshelby tensor is obtained in general, i.e. it is solved for, is it known a-priori (e.g. from Mura, 1987)

*We have added some new sentences here to explain that this tensor is taken as known a-priori based on the previous work of e.g. Mura.*

l. 171, please add “phonon-mode” in the Gruneisen tensor so that this is not confused with the macroscopic definition.

*Added.*

l. 173, please add “(pressure)” after stress, since you are using it later.

*Added.*

l. 238, 256, like in l. 171

*Added. We also checked the rest of the text for similar points.*

l. 283, which “size” you are referring to? The largest? A mean size?

*Revised. We refer to the boundary of the model and the radius of the inclusion.*

l. 370, thus the results using rutile should be viewed with caution since they potentially have large errors.

*Revised as suggested.*

Minor things l. 45: “long time” is relative in geology. I would be more specific, i.e. for more than 50 years

*Revised as suggested.*

l. 139-141, I would break this sentence in smaller parts.

*This sentence is broken into two separate shorter sentences.*

l. 150, I would suggested reformatting, “equals” -> “.. to be equal to..”

*Revised as suggested.*

l. 155, I suppose that this is actually a system of equations that gives you all the eigenstrain components. I would add some brackets here to emphasize this point.

*The reviewer is right and we have changed ‘equation’ into ‘system of equations’.*

l. 204, I would rather replace “space” with “medium”

*Revised as suggested.*

l. 290, Please give the formula of Root Mean Square in the text or in Appendix

*The definition of RMSD is now given in the bracket at its first appearance in the main text.*

l. 560, “is aligned” -> “are aligned”

*Corrected.*

l. 567, please add in brackets the garnet composition (e.g. alm)

*Revised. We just call it almandine garnet.*

l. 570 as in l. 171

*Done.*

## **Reply to comment from R. Angel et al.**

*We thank the workers for posting this interesting comment on the symmetry breaking issue. Below, we provide our replies to the comments. Our replies are given in italic blue and the original comments from the commenters are in black.*

The analysis developed in this manuscript to calculate the Raman shifts developed in ellipsoidal inclusions is correct under the assumption that the symmetry of the inclusion crystal is not broken by the strains imposed by the host crystal. Under these circumstances, it agrees with the extensive analyses published in both the materials science and geological literature.

With an isotropic host crystal (and we agree that normal metamorphic silicate garnets can be treated as being elastically isotropic for these purposes) the Eshelby solution for inclusion stress and strain shows that the symmetry of an ellipsoidal inclusion crystal will be broken when the crystallographic axes of the inclusion crystal do not coincide with the principal axes of its ellipsoidal shape. The manuscript is also correct in stating that the symmetry of faceted inclusion crystals will be also be broken; this is the consequence of stress and strain concentration at corners and edges of the inclusion, as well as of the orientation of the crystallographic axes of the inclusion with respect to the shape. Such symmetry breaking of the inclusion crystal must also affect the values of the components of the phonon-mode Grüneisen tensor which determine its Raman shifts arising from the strains applied to the inclusions. These Grüneisen tensors have only been determined for a limited number of crystals. Recent DFT calculations of these Grünesien tensors (Murri et al. 2018 for quartz; Stangarone et al. 2019 for zircon, Musiyachenko et al. 2020 for rutile) explicitly assume that the symmetry of the crystal is preserved. That means that the unit-cell strains are constrained as  $\epsilon_1 = \epsilon_2$  to preserve the equivalence of the a- and b-axes of these uniaxial crystals. Therefore, these tensors cannot be applied to strain states where the  $\epsilon_1$  component is different from  $\epsilon_2$ , or those with non-zero shear components, which will arise from the mechanical states presented in Figures 4 and 5 of this manuscript.

The magnitude of the effect of symmetry-breaking on the Grüneisen tensors of minerals has not been calculated in recent DFT simulations. But there is direct experimental evidence that it can be significant compared to the shifts without symmetry breaking (e.g. Briggs and Ramdas, 1977, on quartz). If symmetry-breaking was not an issue, then the Raman peaks of cubic host minerals such as diamond and garnets would not exhibit any change in the deviatoric strain fields around inclusions (e.g. Angel et al. 2019). But the Raman shifts in diamond (e.g. Nasdala et al., 2005) and garnets (Campomenosi et al., 2020) around inclusions have been measured and are significant. They are correlated with the symmetry-breaking visible in thin sections as optical birefringence haloes. Therefore, the calculations in the current manuscript of Raman shifts of inclusions whose symmetry is broken is not correct. The magnitude of the error is unknown. In summary, for the cases in which the symmetry of the inclusion crystal is not broken, this manuscript provides results that are in agreement with previous studies with a variety of methods. For inclusions whose symmetry is broken, this manuscript does not allow for the additional Raman shifts that will arise from the symmetry breaking. This means that Figures such as 4 and 5 should not be used to interpret the Raman shifts in quartz inclusions trapped in garnets and the authors should clearly identify in the manuscript all of their examples and calculations in which the inclusion symmetry is broken.

*We agree with the commenters that deviatoric stresses will generally impose an effect of the physical properties of minerals. The commenters also correctly point out that the DFT calculation performed by Murri et al. (2018) embeds the property of  $e_1=e_2$ , which mimics the  $D_3$  symmetry of quartz. We presume that the commenters argue that when our model predicts  $e_1 \neq e_2$ , the existing parameterization of the Grüneisen tensor by Murri et al. (2018) should not be applied as the assumption taken before is violated.*

*First, we want to clarify that the stress-induced symmetry breaking and related impact on physical properties have no adverse effect on the proposed analytical solution based framework to studying inclusion-host mechanics. In our view there are two aspects of the problems: 1) the applicability of the analytical solution and the stress field associated with loads due to inclusion eigenstrain (the main target of the work) and 2) the impact of potential symmetry breaking on the calculated Raman shift. The commenters are mainly concerned*

about the second part. However, the main outcome of our work, which is the proposed analytical solution framework, is largely unaffected by the stress-induced symmetry-breaking effects. Regarding the symmetry breaking issue, it is not only the Gruneisen tensor that is affected by the symmetry breaking effects due to the presence of general (deviatoric) stress states, when for example shear stress components along the principal crystallographic axes do not necessarily vanish. Any physical property such as elastic stiffness, viscosity and thermal expansivity etc. is affected as well, and, in general, resulting in substantial challenges as experimental measurements under different level of deviatoric stress need to be performed and fit all the physical properties as a function of individual stress components. To our knowledge, there is no such data related to e.g. quartz in garnet system. As we are not specialists in experiments, there may be technical difficulties associated with such experiments, which the commenters may know better. However, the proposed analytical approach is capable of incorporating an arbitrary stiffness tensor for the inclusion phase, and in particular the cases of oblique crystallographic orientations with respect to the principal geometric axes of the inclusion. The model, in its incremental form, can also embed stress-induced changes to the stiffness tensor, including the effect due to symmetry-breaking (please see below). In fact, the non-linearity of stiffness tensor (both inclusion and host) due to deviatoric stress has not been addressed in any of the available mechanical models relevant to Raman elastic thermobarometry. The analytical framework described in this work has a capacity to deal with this problem for the inclusion phase (however admittedly not for the host phase), and experimental parametrizations of the non-linear dependence of the mineral stiffness tensor components on general (deviatoric) stress states would be greatly appreciated in this context.

The key question is how large the effects due to symmetry-breaking could be in minerals. The commenters referenced the paper of Briggs and Ramdas (1977), where they applied uniaxial stress on single quartz crystal along  $x$ ,  $y$  and  $z$  direction to fit the experimental deformation potential (same as Gruneisen tensor components). When the uniaxial force  $F$  is along the  $x$  or  $y$  direction, the symmetry is reduced from  $D_3$  to  $C_2$  (or  $C_1$  if  $F$  has arbitrary orientation). In this case, the commenters argue that the Gruneisen tensor should significantly

vary. Below, we summarize the experimentally (uniaxial stress) calibrated Gruneisen components with symmetry broken ( $e_1 \neq e_3$ ) and the HF/DFT ab-initio results from Murri et al. (2019). For comparison purpose, we present the ratio between the Gruneisen components along the crystallographic  $a$  and  $c$  directions. (EXP represents the experimental value from Briggs and Ramdas 1977 and DFT represents the ab-initio results from Murri et al. 2019). Only A1 vibration mode is reported here.

Raman bands	$a/c$ (EXP)	$a/c$ (DFT)
464 (A1)	0.542	0.504
206 (A1)	0.889	0.693
360 (A1)	-0.550	-0.689
1080 (A1)	0	0.06

Although the exact ratio is different, they are still quite comparable and we need to also note that one set is experimental and the other is ab-initio, which is already in good agreement. The experimental data is obtained under uniaxial stress with symmetry broken while the DFT is based on symmetry preserving condition. It is our speculation that the effect of deviatoric stress may not be significant to the Raman shift (also the second-order effect of shear modulus as a function of deviatoric stress). It is also noted that quartz in garnet system has been successfully in numerous literatures cited in the manuscript, showing that the deviatoric stress effect is not so significant at least for quartz case.

We agree that by breaking the mineral symmetry due to applied deviatoric stress, all physical properties, including the Gruneisen and stiffness tensors, may be affected but the amount of the effect is unknown yet due to the lack of experimental data. We would argue that the symmetry breaking effects can be viewed as a subset of a wider class of effects due to stress-induced (non-linear) changes of physical properties. We agree that these effects should be thoroughly studied and the resulting new parameterization could be directly used in improved mechanical models such as the one proposed in this study.

We have added a new paragraph in the manuscript to speculate about the effect of symmetry breaking. We also would like to point out that we are primarily focused how large the departure of Raman shift is from a spherical case by assuming that the phonon coefficients in front of the  $e_1$  and  $e_2$  terms are still the same even if  $e_1$  is not equal to  $e_2$ . This is a first-order

*estimate that is taken here and clarified in the main text. We would be very happy to apply the new calibrations for symmetry broken situation, if they are available, thus we will keep track of the updates of the commenters' research.*

## **References**

Angel RJ, Murri M, Mihailova B, Alvaro M (2019) Stress, strain and Raman shifts. *Zeitschrift für Kristallographie*, 234, 129-140.

Briggs RJ, Ramdas AK (1977) Piezospectroscopy of the Raman spectrum of  $\alpha$ -quartz. *Physical Review B*, 16, 3815-3826.

Campomenosi N, Mazzucchelli ML, Mihailova B, Angel RJ, Alvaro M (2020) Using polarized Raman spectroscopy to study the stress gradient in mineral systems with anomalous birefringence. *Contributions to Mineralogy and Petrology*, 175:16.

Murri, M., Mazzucchelli, M.L., Campomenosi, N., Korsakov, A. V., Prencipe, M., Mihailova, B.D., Scambelluri, M., John, A.R., Matteo, A., Angel, R.J., Alvaro, M., (2018) Raman elastic geobarometry for anisotropic mineral inclusions. *Am. Mineral.* 103, 1869–1872.

Musiyachenko KA, Murri M, Prencipe M, Angel RJ, Alvaro M (2020) A new Grüneisen tensor for rutile and its application to host-inclusion systems. *American Mineralogist*, submitted.

Nasdala, L., Hofmeister, W., Harris, J.W., and Glinnemann, J. (2005) Growth zoning and strain patterns inside diamond crystals as revealed by Raman maps. *American Mineralogist*, 90, 745–748.

Stangarone C, Alvaro M, Angel R, Prencipe M, Mihailova BD (2019) Determination of the phonon-mode Grüneisen tensors of zircon by DFT simulations. *European Journal of Mineralogy*, 31, 685-694

## **Reply to reviewer #2**

The manuscript of Zhong et al. presents analytical and numerical solutions for the deformation and stress of ellipsoidal inclusions in an infinite host. These solutions are applied to so-called Raman elastic thermobarometry, which is a method to estimate the peak P-T conditions of exhumed rocks. This thermobarometry is an alternative method with respect to P-T estimates based on thermodynamic Gibbs energy minimizations and is, hence, important to validate and cross-check P-T estimates obtained from different methods. The authors present solutions for an anisotropic inclusion in anisotropic host and further present approximate solutions for so-called faceted inclusions (inclusions with corners). The analytical solutions are tested with numerical simulations based on the finite element method. The Raman elastic thermobarometry is an important and more and more applied method to estimate P-T conditions of exhumed rocks and is, hence, of interest for a wide readership. The authors also provide several of their numerical algorithms, which allows readers to reproduce the presented results and to apply these algorithms for their own research. The open access to these algorithms is a great benefit of this contribution.

However, the authors should discuss in more detail the limits of applicability of their solutions and potential magnitudes of errors when applied to natural host-inclusion studies, which are likely more complex. Ideally, the authors should provide something like a “check-list” for the application of their solution to natural host-inclusion systems.

*We have added a new section “5. Limitation of applicability” to discuss this issue as suggested by the reviewer. This includes the discussion and limitation of some of the assumptions that we have taken so far, e.g. infinite and isotropic host, linear-elasticity and inclusion shape. This is practically a check list to remind readers of the potential issues of elastic thermobarometry, and we believe there will be certainly more refinement to work on in the future.*

I have also read the comment to this manuscript by Angel et al., which discusses in detail some limits of the presented models, for example arising due to different orientations of the

axes of crystallographic orientations and the principal axis of the ellipsoidal shape. I find this comment very useful and urge the authors to clearly explain and discuss these limitations.

*We have provided a detailed reply to Angel et al. and added new text into the manuscript to address this issue. We agree that this is worth mentioning but, in our view, the symmetry breaking issue has no adverse effect on our work: 1) Its estimated effect on the final Raman shift seems minor after comparing the experimental and DFT calculations (see table above in the reply to Angel et al.). 2) Obtaining the Raman shift using residual strain or stress is intrinsically a post-processing procedure that does not affect our analytical solution at all (so our main focus is not impacted). 3) Lastly, there are simply no available parameterizations of the physical properties such as elastic stiffness, thermal expansivity and particularly the Gruneisen tensor under non-symmetric deviatoric stress.*

Making algorithms available is great for the research community, but always generates the risk that users may apply such algorithms wrongly to natural systems for which the algorithms are actually not correctly applicable. Therefore, the authors should address the limitations and applicability of their solutions in detail during a revision of their manuscript. Apart from this major comment, I have a few minor comments, which the authors might also consider during a revision.

**Minor comments:**

Line 86-88: These are strong assumptions for the stage of entrapment. Maybe these assumptions could be discussed and justified in the Discussion section.

*We agree with the reviewer that we use an assumption that upon entrapment, the inclusion and host were subject to the same stress field. However, it can be argued that this assumption is a reasonable one considering that when the inclusion was engulfed by the host during its growth, they must possess the same stress state under mechanical equilibrium as elastic stress equilibration is a fast process compared to mineral growth. This is made clear in the main text after this sentence.*

Line 97: For readers not expert in anisotropy in minerals, it would be useful to explain the angles, maybe even with a little sketch showing the anisotropy axes and the corresponding angles.

*We have added a sentence explaining the meaning of the angles.*

Line 107: Please explain what the PVT relationship is. Best would be to just add the formula to avoid any ambiguity.

*We have added a line describing the PVT relationship. It is difficult to add a simple formula to describe the relationship because: 1) there are many distinct PVT relationships, each applied to different minerals; 2) the relationships are highly non-linear and often implicit, so it is not possible to use one simple formula to describe the PVT relationship. Therefore, we have not added any specific PVT formula to avoid potential confusion.*

Line 171: Could you add a sentence explaining the origin of the Grüneisen tensor for the non-specialists. For example, is this tensor derived from theoretical calculations or determined from experiments?

*Done. We have added new text here to describe this tensor. Both ab-initio and experimental data on the Gruneisen tensor exist and they seem to match quite well, even if they are done at distinct stress condition. See the table in the reply to Angel et al.*

Line 214: A main result is quantifying the impact of the aspect ratio. However, the impact of the aspect ratio is not very transparent from the presented equations. Is there a possibility to provide an equation, which shows the impact of the aspect ratio on the Eshelby tensor clearer, or in a more transparent way?

*There is unfortunately no explicit form describing the impact of aspect ratio on the Eshelby tensor (not to mention the final expression for the residual stress), e.g. see the work of Mura 1987, who has attempted and the current formula is at its most simplified form as given in the Appendix. Therefore, we did not change this part.*

Line 235-231: Could you provide a simple and/or intuitive explanation why the aspect ratio is least sensitive for quartz but most sensitive for rutile. What is the controlling mechanical difference between quartz and rutile responsible for the different sensitivity?

*It's not very intuitive why the rutile is more sensitive to aspect ratio as it requires deriving an explicit form of stress variation from spherical case due to shape change, which cannot be easily done. One possibility is that rutile is highly anisotropic, which makes the residual stress more sensitive to the change of aspect ratio. We have added this into the text. However, we also noted that care must be taken for this explanation because we have not tested all minerals and in case of other minerals, readers are encouraged to perform their own calculation.*

Line 242: Could you provide a typical value of a wavenumber variation, which “defines” the transition from significant to insignificant variation? Maybe as percentage with respect to the corresponding Raman peak.

*We have added a sentence here to clarify this point. The main point is that as long as the variation stays below the detection limit of standard Raman machine after Gaussian fitting of the Raman band position (e.g.  $0.2 \text{ cm}^{-1}$ ), we consider the effect insignificant. This is made clear in the main text now.*

Line 272: Please add a sentence explaining what the second-order moment is and why the second-order moment is needed and not the first-order moment.

*We have removed the second-order moment to simplify the text for readers. It is practically a method that minimize the mismatch between the irregular inclusion shape with the effective ellipsoid.*

Line 305: So I guess “interestingly” implies that you did not expect such better approximation. Could you provide now an explanation why you got this better approximation, or do you still not know why this approximation is better?

*This is an observation that volumetric stress average provides a better approximation than the central point. This is interesting that this measure is better considering the fact that when*

*performing Raman measurement on inclusions, we are in fact averaging over the effective volume under the laser. Therefore, it is interesting and, in fact, useful that the average volume is a better proxy than just a central point. For an explanation, we can so far provide a speculation that it is due to the consideration of the stress variations at the inclusion-host wall (on the inclusion side) that drive the volumetric average closer to the equivalent stress based on the effective ellipsoid. However, it is difficult to prove it because the inclusion shape is arbitrary and faceted so there is no easy analytical description of the stress field.*

Line 389: comma instead of point.

*Corrected.*

Conclusions: The conclusion section could be shortened by stating only the main conclusions and the main new results.

*We have slightly shortened the last section. However, this section is more inclined to geological implications to provide a summary for the geologists who might not be interested in the mathematical derivations, but only the geological relevance. Therefore, we still prefer to keep most of the text so that it is easier to follow and readers may hopefully benefit more for their own petrological works.*

Numerical codes: The Matlab script “Fit\_Ellipsoid” uses, for example, the command “syms” which requires the Symbolic Math Toolbox; so this script cannot be run with a basic Matlab license. It would be great if the authors could modify the codes, if possible, so that they can be used also with a basic Matlab student license.

*We thank the reviewer for reminding us this issue. We have revised the code so that now it does not need the symbolic toolbox and everyone with basic MATLAB can use it. We now use the function handle, which is available with standard MATLAB version.*

# Analytical solution for residual stress and strain preserved in anisotropic inclusion entrapped in isotropic host

Xin Zhong<sup>1,2</sup>, Marcin ~~Dabrowski~~<sup>2</sup>~~Dabrowski~~<sup>2,3</sup>, Bjørn Jamveit<sup>2</sup>

1. Institut für Geologische Wissenschaften, Freie Universität Berlin, Malteserstrasse 74–100, 12449 Berlin, Germany

5 2. Physics of Geological Processes, The Njord Center, University of Oslo, Norway

3. Computational Geology Laboratory, Polish Geological Institute - NRI, Wrocław, Poland

Correspondence to: Xin Zhong (xinzhong0708@gmail.com)

**Abstract.** Raman elastic thermobarometry has recently been applied in many petrological studies to recover the pressure-temperature ( $P$ - $T$ ) conditions of mineral inclusion entrapment. Existing modelling methods in petrology either adopt an assumption of a spherical, isotropic inclusion embedded in an isotropic, infinite host, or use numerical techniques such as finite element method to simulate the residual stress and strain state preserved in the non-spherical anisotropic inclusion. Here, we use the Eshelby solution to develop an analytical framework for calculating the residual stress and strain state of an elastically anisotropic, ellipsoidal inclusion in an infinite, isotropic host. The analytical solution is applicable to any class of inclusion symmetry and an arbitrary inclusion aspect ratio. Explicit expressions are derived for some symmetry classes including e.g. tetragonal, hexagonal and trigonal.

The effect of changing the aspect ratio on residual stress is investigated including quartz, zircon, rutile, apatite and diamond inclusions in garnet host. Quartz is demonstrated to be the least affected, while rutile is the most affected. For prolate quartz inclusion ( $c$ -axis longer than  $a$ -axis), the effect of varying the aspect ratio on Raman shift is demonstrated to be insignificant. When  $c/a=5$ , only ca.  $0.3 \text{ cm}^{-1}$  wavenumber variation is induced as compared to the spherical inclusion shape. For oblate quartz inclusions, the effect is more significant, when  $c/a=0.5$  ca.  $0.8 \text{ cm}^{-1}$  wavenumber variation for the  $464 \text{ cm}^{-1}$  band is induced compared to the reference spherical inclusion case. We also show that it is possible to fit an effective ellipsoid to obtain a proxy for the averaged residual stress/strain within faceted inclusion. The difference between the volumetrically averaged stress of a faceted inclusion and the analytically calculated stress from the best-fitted effective ellipsoid is calculated to obtain the root mean square deviation (RMSD) for quartz, zircon, rutile, apatite and diamond inclusions in garnet host. Based on the results of 500 randomly generated (a wide range of aspect ratio and random crystallographic orientation) faceted inclusion, we show that the volumetrically averaged stress serves as an excellent stress measure and the associated RMSD is less than 2%, except for diamond-in-garnet system with a systematically higher RMSD (ca. 8%). This expands the applicability of the analytical solution for any arbitrary inclusion shape in practical isotropic host for Raman measurements.

## 30 1. Introduction

Raman elastic thermobarometry has been extensively used to recover the pressure and temperature ( $P$ - $T$ ) conditions of mineral inclusion entrapment, e.g. the mostly studied quartz-in-garnet inclusion-host pair (Ashley et al., 2014; Bayet et al., 2018; Enami et al., 2007; Gonzalez et al., 2019; Kouketsu et al., 2014; Taguchi et al., 2016, 2019; Zhong et al., 2019). (Ashley et al., 2014; Bayet et al., 2018; Enami et al., 2007; Gonzalez et al., 2019; Kouketsu et al., 2014; Taguchi et al., 2016, 2019; Zhong et al., 2019b). Recently, quartz-in-garnet elastic barometry has been calibrated with experiments by synthesizing almandine garnets and quartz inclusions at high  $P$ - $T$  conditions and comparing the entrapment pressure recovered based on residual pressure measured in quartz with the pressure applied in experiments (Bonazzi et al., 2019; Thomas and Spear, 2018). In practice, most mineral inclusions, e.g. quartz, zircon and rutile, are elastically anisotropic, and Given the associated residual stress or strain state, the anisotropic effect needs to be addressed/considered for better constraining/recovering the entrapment  $P$ - $T$  conditions. Existing mechanical models for elastic thermobarometry typically assume the case of a spherical isotropic inclusion entrapped in an infinite isotropic host (e.g. Angel et al., 2017b; Gillet et al., 1984; Guiraud and Powell, 2006; Rosenfeld and Chase, 1961; Zhang, 1998). In recent studies, finite element (FE) simulations were applied to study anisotropic inclusions entrapped in cubic hosts such as garnet (Alvaro et al., 2020; Mazzucchelli et al., 2019). In this approach, the residual strain preserved within a mineral inclusion is related to the stress/strain state of the system upon entrapment via a relaxation tensor ( $R$ ) that needs to be pre-calculated using the FE method or other numerical techniques (Mazzucchelli et al., 2019).

For an ellipsoidal, elastically anisotropic inclusion entrapped in an infinite isotropic host, an exact closed-form analytical solution is available for a long time more than 50 years (Eshelby, 1957; Mura, 1987). This solution has been widely applied to the earth science for many problems, such as viscous creep around inclusions (Freeman, 1987; Jiang, 2016); flanking structures (Exner and Dabrowski, 2010); elastic stress of inclusions at various scales (Meng and Pollard, 2014); microcracking and faulting (Healy et al., 2006), magma chamber induced deformations (Bonaccorso and Davis, 1999) etc. The advantage of such form is that no numerical software or programming is required and the solution is exact (no numerical error) and can be obtained rapidly and precisely, with no numerical approximation error. The rapid calculation also permits in-depth, systematic stress and strain analysis of inclusion-host system or potentially Monte-Carlo simulation for uncertainty propagation (e.g. Anderson, 1976). The procedure of calculating the residual stress in an ellipsoidal anisotropic inclusion embedded in an elastic, isotropic host is based on the equivalent eigenstrain method and the classical Eshelby solution (Eshelby, 1957; Mura, 1987). Recently, the Eshelby's solution has been applied to exhumed mineral inclusion entrapped in a host and the result is compared to the finite element method (Morganti et al., 2020). Mineral inclusions were measured for their crystallographic orientation and shape via X-ray diffraction and tomography (Morganti et al., 2020), but the significance of the aspect ratio, shape and crystallographic orientation have not been studied in a systematic way. More importantly, the Eshelby's solution only applies to perfectly ellipsoidal inclusions but natural mineral inclusions are faceted. Therefore, the uncertainty and limitation of using the Eshelby's solution to natural faceted inclusions remain to be investigated. In this study, we attempt to explore in-depth the Eshelby's solution to inclusion-host problem. A general analytical form is first presented in this paper (previous submission

record available in Acknowledgements) following the Eshelby's equivalent eigenstrain method (Mura, 1987, chapter 4) to calculate residual stress and strain of an anisotropic inclusion in an isotropic host. For inclusions belonging to certain crystallographic symmetry, such as tetragonal, hexagonal and trigonal, simplified explicit expressions describing residual stress and strain are derived. The analytical formulas are cross validated against the numerical results obtained using a self-developed finite element code. Convergence tests are successfully performed to show the correspondence of the numerical (FE) and analytical solution. In-depth analysis of the effects due to: 1) inclusion elastic anisotropy, 2) inclusion aspect ratio, 3) relative orientation between the inclusion crystallographic and geometrical principal axis, are performed to show how they affect the application of elastic thermobarometry. ~~The All MATLAB code has also~~ codes necessary for performing the analytical solution have been made available together with the submission- (see the main codes in Appendix).

One major problem of using the Eshelby's solution to mineral inclusion is that natural inclusions are faceted in shape, which leads to a heterogeneous residual stress field (e.g. Chiu, 1978; Mazzucchelli et al., 2018). To resolve this issue, we use our self-developed 3D finite element code to simulate the residual stress distribution within faceted inclusions of varying shapes. Fitting an arbitrary 3D shape with effective ellipsoid is a common practice in image analysis and microstructural research (e.g. Ghosh and Dimiduk, 2011). We explore the possibility of using an effective ellipsoid to approximate the shape of a faceted inclusion. The residual stress obtained from the analytical solution based on the best-fitted effective ellipsoid is used as a proxy to represent the volumetrically averaged stress within the faceted inclusion. By inspecting the numerical (FE) and analytical solutions, we have found that for most mineral inclusions, e.g. quartz, zircon, apatite and rutile, the volumetrically averaged stress represents very well the stress state of arbitrarily faceted inclusions. This may potentially provide useful guides to the future applications of elastic thermobarometry for any natural faceted mineral inclusions.

## 2. Method

### 2.1 Anisotropic inclusion embedded in isotropic host

We consider an anisotropic, ellipsoidal solid inclusion entrapped in an isotropic, infinite host at high  $P$ - $T$  conditions. For a fully entrapped spherical inclusion, the assumption of an infinite host is justified when the distance between the inclusion and host grain outer boundaries, such as the thin-section surface, is more than 3 times the inclusion radius (Mazzucchelli et al., 2018; Zhong et al., 2018)-(Mazzucchelli et al., 2018; Zhong et al., 2019a). The principal axes of the inclusion are aligned along the Cartesian coordinates  $x$ ,  $y$  and  $z$ , and their lengths are arbitrary. Upon entrapment at depth, it is considered that the inclusion and host are subject to the same stress field. This is justified in the situation when the inclusion was first formed and the host grew to engulf the inclusion at high  $P$ - $T$  conditions and this process occurred slowly so that mechanical equilibrium was satisfied all the time. In the text, it is not discussed if the inclusion and host grew under different (but mechanically equilibrated) stress field upon entrapment. The entrapment stress may be either hydrostatic or non-hydrostatic but it is treated to be homogeneous during the inclusion growth within the host grain or the overgrowth of the inclusion by the host grain. At this stage, the lattice strains of the inclusion and host are denoted by  $\epsilon_i^{\text{incl}}$  and  $\epsilon_i^{\text{host}}$ , which are measured with respect to the

95 reference room conditions. The Voigt notation is applied here (Voigt, 1910). The entrapment lattice strains  $\epsilon_i^{\text{incl}}$  and  $\epsilon_i^{\text{host}}$  incorporate both pressure (compressibility) and temperature (thermal expansivity) effects. They can be obtained by relating the lattice parameters measured at high  $P$ - $T$  conditions to their reference values under room  $P$ - $T$  condition. For inclusions of cubic, tetragonal and orthorhombic symmetry classes, the three crystallographic axes  $a$ ,  $b$  and  $c$  are mutually perpendicular to each other, so that the lattice strain  $\epsilon_i^{\text{incl}}$  can be readily expressed as:

$$\begin{aligned}\epsilon_{xx}^{\text{incl}} &= \frac{a}{a_0} - 1 \\ \epsilon_{yy}^{\text{incl}} &= \frac{b}{b_0} - 1 \\ \epsilon_{zz}^{\text{incl}} &= \frac{c}{c_0} - 1\end{aligned}\tag{1}$$

100 where e.g.  $a_0$  is the reference lattice parameter measured at room conditions and  $a$  is the lattice parameter measured at entrapment conditions. Note that for hexagonal and trigonal minerals (e.g. quartz), if the symmetry of lattice parameters is maintained at entrapment conditions (e.g. for quartz we keep  $a=b$ ,  $\alpha = \beta = 90^\circ$ ,  $\gamma = 120^\circ$ ), Eq. 1 still holds. For lower symmetry systems with non-orthogonal crystallographic axes (triclinic and monoclinic systems), it's not possible to align all the crystallographic axes parallel to the Cartesian coordinates and the angles of  $\alpha$ ,  $\beta$  and  $\gamma$  may also change at entrapment condition compared to reference room condition. Therefore, transformation is needed to convert strains from the crystallographic axes in a unit cell to the Cartesian coordinate system for modelling the mechanical interaction between the inclusion and host. This can be done by using existing software such as PASCAL (Cliffe and Goodwin, 2012), Win\_Strain (<http://www.rossangel.com/home.htm>), and STRAIN (Ohashi and Burnham, 1973). A self-written MATLAB code is provided also in the Appendix following the

105 Ohashi's method (Ohashi and Burnham, 1973) to calculate the lattice strain based on the changes of lattice parameters. The results are the same with all existing software. For the case of an isotropic host under hydrostatic entrapment stress, the initial (entrapment) strain is expected to be isotropic and the principal strain components are simply one third of the volumetric strain, which can be directly obtained from the PVT relationship. For the case of an isotropic host under hydrostatic entrapment stress, the initial (entrapment) strain is expected to be isotropic and the principal strain components are simply one third of the volumetric strain, which can be directly obtained from the PVT (pressure-volume-temperature) relationship (e.g. garnet in Milani et al., 2015).

110 Milani et al., 2015).

To simulate the exhumation of the inclusion-host system to room  $P$ - $T$  conditions, we first unload the system by applying the strain opposite to the initial host strain state, i.e.  $-\epsilon_i^{\text{host}}$  (Fig. 1B), a procedure which leads to a stress- and strain-free host at room conditions. This is an intermediate step that ignores elastic interaction between the inclusion and host, and the inclusion will possess a virtual strain  $\epsilon_i^{\text{incl}} - \epsilon_i^{\text{host}}$ , as the internal inclusion-host boundary experiences the unloading strain  $-\epsilon_i^{\text{host}}$ . At this moment, the stress state of the inclusion can be readily expressed using the linear-elastic constitutive law as:  $C_{ij}^{\text{incl}}(\epsilon_j^{\text{incl}} -$

120

Formatted Table

$\epsilon_i^{\text{host}}$ ), where  $C_{ij}^{\text{incl}}$  is the elastic stiffness tensor of the inclusion at room  $T$ . Einstein summation is used. It is straightforward to note that mechanical equilibrium is not satisfied at this intermediate step because, in general, there is a stress jump between the stressed inclusion and the stress-free host. Using the proposed approach, solving the original mechanical problem is reduced to superposing the homogeneous unloading strain field  $-\epsilon_i^{\text{host}}$  with a non-uniform solution for an initially stressed and strained inclusion embedded in a stress and strain free host at room  $T$ . The latter one is practically an eigenstrain problem (Eshelby, 1957). The ~~thermal effects on temperature dependence of~~ the elastic stiffness tensor  $C_{ij}^{\text{incl}}$  have no influence on the superposed deformation field driven by the eigenstrain load due to the mismatch between the lattice strains of the inclusion and the host. The stress and strain of the inclusion that serve as driving force for elastic interaction are as follows:

$$\begin{aligned}\epsilon_i^* &= \epsilon_i^{\text{incl}} - \epsilon_i^{\text{host}} \\ \sigma_i^* &= C_{ij}^{\text{incl}}(\epsilon_j^{\text{incl}} - \epsilon_j^{\text{host}})\end{aligned}\quad (2)$$

where  $\epsilon_i^*$  are referred to as inclusion eigenstrains and  $\sigma_i^*$  are eigenstresses (Mura, 1987). The eigenstresses ~~correspond to can be understood as~~ the ~~stresse~~equilibrated stresses that ~~an infinitely~~ soft inclusion would experience if it was perfectly confined by a ~~stiff~~rigid host, i.e. the host was not allowed to deform elastically. The eigenstrain and eigenstress are the functions of the lattice strain of inclusion and host at entrapment conditions (taking room conditions as reference state) and the stiffness tensor of the inclusion at room  $P$ - $T$  condition.

Because mechanical equilibrium is not satisfied for the stressed inclusion embedded in a stress-free host, elastic deformation will occur (stage shown in Fig. 1b to Fig. 1c). The amount of elastic deformation that affects the inclusion with a pre-strain  $\epsilon_i^{\text{incl}} - \epsilon_i^{\text{host}}$  in a stress-free host to mechanical equilibrium is denoted as  $\epsilon_i$ . The strain  $\epsilon_i$  is shown in Fig. 1b to 1c, and the pre-strained state with strain  $\epsilon_i^{\text{incl}} - \epsilon_i^{\text{host}}$  is taken as the reference state for this elastic deformation field. By adding the strain  $\epsilon_i$  to the inclusion, we obtain the final residual stress and strain state as follows:

$$\begin{aligned}\epsilon_i^{\text{res}} &= \epsilon_i^{\text{incl}} - \epsilon_i^{\text{host}} + \epsilon_i \\ \sigma_i^{\text{res}} &= C_{ij}^{\text{incl}}(\epsilon_j^{\text{incl}} - \epsilon_j^{\text{host}} + \epsilon_j)\end{aligned}\quad (3)$$

where  $\epsilon_i^{\text{res}}$  and  $\sigma_i^{\text{res}}$  are the final residual strains and stresses of the inclusion, which are the true physical stress and strain the inclusion experiences. This final stage is shown in Fig. 1c. Finding the strain  $\epsilon_i$  will solve the anisotropic inclusion problem. This will be sought in the next section using the equivalent eigenstrain method and Eshelby's solution.

## 2.2 Solving the problem with Eshelby's solution

The Eshelby's solution treats a homogeneous, ellipsoidal, isotropic inclusion embedded in an infinite isotropic host (Eshelby, 1957). Following Eshelby (1957), we replace the inclusion-host system by an isotropic homogeneous ~~space~~medium with elastic tensor  $C_{ij}^{\text{host}}$  and ~~load~~loads the ellipsoidal inclusion region with an equivalent eigenstrain  $e_i^*$  (to differentiate from the

previously introduced eigenstrain term  $\varepsilon_i^*$  due to lattice strain mismatch). The equivalent eigenstrain  $e_j^*$  is a yet unknown eigenstrain that load the isotropic inclusion in the same isotropic host so that to create the same stress field as in the previous case where the inclusion is anisotropic. Without elastic interaction, the inclusion would experience a stress  $-C_{ij}^{\text{host}} e_j^*$  under perfect confinement (e.g. a positive eigenstrain (expansion) leads to compressive stress, which is negative). After elastic interaction, the inclusion ~~strain~~ stress ~~host should be~~ under mechanical equilibrium due to a constant eigenstrain (eigenstress) load applied to an ellipsoidal region of otherwise homogeneous elastic ~~space~~ medium. The elastic interaction (from mechanical non-equilibrium to equilibrium) is solved for by using the Eshelby's tensor  $S_{ij}$ , which transforms the inclusion strain from the loaded eigenstrain to the final strain that is under mechanical equilibrium. The residual stress and strain of the inclusion can be expressed as follows (Eshelby, 1957; Mura, 1987):

$$\begin{aligned}\varepsilon_i^{\text{res}} &= S_{ij} e_j^* \\ \sigma_i^{\text{res}} &= C_{ij}^{\text{host}} (S_{jk} e_k^* - e_j^*)\end{aligned}\quad (4)$$

where  $S_{ij}$  is the Eshelby's tensor, which gives the one-to-one mapping between the equivalent eigenstrain ( $e_j^*$ ) and a homogeneous residual strain ( $\varepsilon_i^{\text{res}}$ ) within the inclusion region. The Eshelby's solution is manifested in this tensor, which is only a function of the inclusion shape and the Poisson ratio ( $\nu$ ) of the isotropic host. The detailed derivation of the Eshelby's tensor based on the use of the Green's function can be found in e.g. Mura (1987) (MATLAB code is given to calculate this tensor). For a spherical inclusion,  $S_{ij}$  is symmetric and can be significantly simplified as follows:

$$\begin{aligned}S_{11} = S_{22} = S_{33} &= \frac{7-5\nu}{15(1-\nu)} \\ S_{12} = S_{23} = S_{13} &= \frac{5\nu-1}{15(1-\nu)} \\ S_{44} = S_{55} = S_{66} &= \frac{4-5\nu}{15(1-\nu)}\end{aligned}\quad (5)$$

All the other components are zero. For general ellipsoidal inclusions, the  $S_{ij}$  tensor is given in the Appendix and a MATLAB script for calculating the  $S_{ij}$  tensor is provided in the supplementary materials (see Appendix for more details for using the script).

Following the equivalent eigenstrain method (Mura, 1987, chapter 4), one may appropriately choose the equivalent eigenstrain  $e_j^*$  to let  $S_{ij} e_j^*$  in Eq. 4 equal to be equal to the strain  $\varepsilon_i$  in Eq. 3 that drives the pre-strained anisotropic inclusion into mechanical equilibrium with stress-free isotropic host, i.e. we have:

$$\varepsilon_i = S_{ij} e_j^* \quad (6)$$

By doing so, the stresses in the original anisotropic heterogeneity and the equivalent isotropic inclusion will be equal. This is because the host is stressed (and strained) by the same amount following Eq. 6, which leads to the same inclusion stress because the traction is matched between inclusion and host. By replacing the strain  $\varepsilon_i = S_{ij}e_j^*$  into  $\sigma_i^{\text{res}}$  in Eq. 3 and equating the [system of equations containing the stresses  \$\sigma\_i^{\text{res}}\$](#)  in Eq. 3 with [those in](#) Eq. 4, we obtain the following relation:

$$\sigma_i^{\text{res}} = C_{ij}^{\text{incl}}(\varepsilon_j^{\text{incl}} - \varepsilon_j^{\text{host}} + S_{jk}e_k^*) = C_{ij}^{\text{host}}(S_{jk}e_k^* - e_j^*) \quad (7)$$

The equivalent eigenstrain  $e_k^*$  can be solved from this equation. By substituting the obtained  $e_k^*$  back into Eq. 7, we may concisely express the final result for the residual strain and stress of the anisotropic inclusion embedded in isotropic infinite host:

$$\begin{aligned} \varepsilon_i^{\text{res}} &= (I_{ij} - M_{ij})\varepsilon_j^* \\ \sigma_i^{\text{res}} &= C_{ik}^{\text{incl}}(I_{kj} - M_{kj})\varepsilon_j^* \end{aligned} \quad (8)$$

where  $I_{ij}$  is the identity matrix. The dimensionless matrix  $M_{kj}$  can be expressed as follows:

$$M_{ij} = [C_{ik}^{\text{incl}} - C_{il}^{\text{host}}(I_{lk} - S_{lk}^{-1})]^{-1} C_{kj}^{\text{incl}} \quad (9)$$

The dimensionless matrix  $M_{ij}$  depends on the elastic stiffness properties of the inclusion and the host as well as the aspect ratio of the inclusion manifested by the Eshelby's tensor. The components of this matrix are close to zero for a stiff host or a soft inclusion (no elastic relaxation so that  $\sigma_i^{\text{res}} \rightarrow C_{ij}^{\text{incl}}\varepsilon_j^*$ ) and it approaches the identity matrix for an infinitely soft host (in this case,  $\sigma_i^{\text{res}} \rightarrow 0$ ). An extreme case is represented by gas/liquid inclusion whose  $C_{ij}^{\text{incl}}$  is low compared to the host stiffness, thus this dimensionless matrix  $M_{ij}$  approaches zero and the isochoric assumption for the gas/liquid inclusion is justified. The  $M_{ij}$  matrix can be readily calculated by using the published elastic stiffness tensor at room  $P$ - $T$  conditions (e.g. Bass, 1995). A MATLAB script is given in the supplementary data to perform this task (details of using the code can be found in Appendix)

### 2.3 Back-calculating eigenstrain terms based on residual inclusion strain

The wavenumber shifts of Raman peaks are induced by lattice strain. By measuring wavenumber shift of the inclusion in a thin-section, it is possible to recover the residual strain preserved within the inclusion (Angel et al., 2019; Murri et al., 2018).

~~This can be done by using the Grüneisen tensor.~~ This can be done by using the phonon-mode Grüneisen tensor, which is typically calculated using *ab-initio* methods such as Hartree-Fock/Density Functional Theory (HF/DFT). Experimental methods have also been applied to quantify such properties under uniaxial stress (called deformation potential in e.g. Briggs and Ramdas, 1977). Therefore,  $\varepsilon_i^{\text{res}}$  can be obtained with e.g. least-square fitting method (Murri et al., 2018) and the residual stress (or pressure) can be readily expressed as  $\sigma_i^{\text{res}} = C_{ij}^{\text{incl}}\varepsilon_j^{\text{res}}$ .

190 By inverting the right-hand matrix in Eq. 8, the eigenstrain terms can be expressed as a function of residual strain  $\epsilon_i^{\text{res}}$ :

$$\epsilon_i^* = \left\{ 1 - (I_{jl} - S_{jl}^{-1})^{-1} C_{ij}^{\text{host}^{-1}} C_{ik}^{\text{incl}} \right\} \epsilon_k^{\text{res}} \quad (10)$$

For tetragonal or hexagonal minerals, e.g. zircon, rutile and apatite, the stiffness tensor comprises six independent components:  $C_{11}^{\text{incl}}, C_{12}^{\text{incl}}, C_{13}^{\text{incl}}, C_{33}^{\text{incl}}, C_{44}^{\text{incl}}, C_{66}^{\text{incl}}$ . For trigonal symmetry such as in the case of  $\alpha$ -quartz, another independent component  $C_{14}^{\text{incl}} = -C_{24}^{\text{incl}}$  is also present. For all these mineral inclusions, and for axially symmetric residual strains,  $\epsilon_i^*$  can be significantly simplified as follows ( $\epsilon_x^* = \epsilon_y^* \neq \epsilon_z^*$ ):

$$\begin{aligned} \epsilon_x^* &= \epsilon_x^{\text{res}} + \frac{5(1-\nu)}{2(7-5\nu)} \left[ (\bar{C}_{11}^{\text{incl}} + \bar{C}_{12}^{\text{incl}}) \epsilon_x^{\text{res}} + \bar{C}_{13}^{\text{incl}} \epsilon_z^{\text{res}} \right] - \frac{3-5\nu}{4(7-5\nu)} (2\bar{C}_{13}^{\text{incl}} \epsilon_x^{\text{res}} + \bar{C}_{33}^{\text{incl}} \epsilon_z^{\text{res}}) \\ \epsilon_z^* &= \epsilon_z^{\text{res}} - \frac{3-5\nu}{2(7-5\nu)} \left[ (\bar{C}_{11}^{\text{incl}} + \bar{C}_{12}^{\text{incl}}) \epsilon_x^{\text{res}} + \bar{C}_{13}^{\text{incl}} \epsilon_z^{\text{res}} \right] + \frac{13-15\nu}{4(7-5\nu)} (2\bar{C}_{13}^{\text{incl}} \epsilon_x^{\text{res}} + \bar{C}_{33}^{\text{incl}} \epsilon_z^{\text{res}}) \end{aligned} \quad (11)$$

195 where  $\bar{C}_{ij}^{\text{incl}} = C_{ij}^{\text{incl}}/G$  is the dimensionless inclusion stiffness tensor scaled by the host shear modulus. [Spherical inclusion is considered here](#). Interestingly, for trigonal  $\alpha$ -quartz inclusions ( $C_{14}^{\text{incl}} \neq 0$ ), the stiffness tensor component  $C_{14}^{\text{incl}}$  is not present in the expression given by Eq. 11. In fact, the terms in the brackets are simply the residual stress components:

$$\begin{aligned} \epsilon_x^* &= \epsilon_x^{\text{res}} + \frac{5(1-\nu)}{2G(7-5\nu)} \sigma_x^{\text{res}} - \frac{3-5\nu}{4G(7-5\nu)} \sigma_z^{\text{res}} \\ \epsilon_z^* &= \epsilon_z^{\text{res}} - \frac{3-5\nu}{2G(7-5\nu)} \sigma_x^{\text{res}} + \frac{13-15\nu}{4G(7-5\nu)} \sigma_z^{\text{res}} \end{aligned} \quad (12)$$

By substituting the stiffness tensor components and the measured residual strains, the eigenstrains can be directly calculated. The equation above thus allows estimation of the entrapment (hydrostatic or non-hydrostatic) stress (or strain) conditions by known the residual stress and strain conditions of the inclusion.

### 3. Cross validation against finite element solution

We have validated our implementation of the proposed analytical framework against independent finite element (FE) solutions. A self-written 3D FE code is used to validate the presented analytical solution ([Dabrowski et al., 2008](#); [Zhong et al., 2018](#)), ([Dabrowski et al., 2008](#); [Zhong et al., 2019a](#)). For validation purposes, we used spheroidal quartz inclusions in an almandine garnet host. Adaptive tetrahedral computational meshes, with the highest resolution within and around the inclusion, are generated with *Tetgen* software (Si, 2015). The anisotropic elastic properties of quartz inclusion at room  $T$  are based on Heyliger et al. (2003). The host garnet elasticity is first treated as isotropic based on Jiang et al. (2004). The model length is set as 10 times (denoted as \*10 below) the inclusion's diameter (for spheroidal inclusion case, the model domain is a box where the side lengths are proportional to the corresponding axes lengths of the inclusion). For the model validation, we adjust the eigenstrain term to generate precisely 1 GPa compressive residual stress for spherical inclusion in infinite garnet host. This is done by letting  $\sigma_{xx}^{\text{res}} = \sigma_{yy}^{\text{res}} = \sigma_{zz}^{\text{res}} = -1$  GPa hydrostatically and substituting  $\sigma_i^{\text{res}}$  into Eq. 8 to back-calculate the

eigenstrain  $\epsilon_j^*$ . Then, the spheroidal inclusion is loaded by the calculated eigenstrain  $\epsilon_j^*$  in the FE code, and the residual stress is compared to results obtained by the presented analytical solution. The choice of eigenstrains (either loading the inclusion to 1 GPa pressure or any other residual stress value) is not influential for the validation purposes, as long as both the analytical and FE methods take the same eigenstrains. This and other successful, more general tests with arbitrary aspect ratio and eigenstrains, have been performed but are not reported here.

In Fig. 2a, the numerically and analytically obtained residual stresses are plotted together as a function of the aspect ratio of the tested spheroidal inclusions. In Fig. 2b, the difference is plotted as a function of element count and boundary distance (\*5, \*10 and \*20). It is clearly shown that the two sets of solutions converge with increasing the number of mesh elements and the computational box size. The success of this convergence test validates the correctness of our presented analytical model (also FE code) for an anisotropic ellipsoidal inclusion entrapped in an isotropic ~~space~~medium.

In addition, we have also tested the effect of applying cubic elastic stiffness tensor of almandine from Jiang et al. (2004) and compared the residual stress with the results obtained for an elastically isotropic garnet (blue dots in Fig. 2a). The difference in residual stresses obtained with FE method using anisotropic garnet host and the analytical solution (implicitly assuming isotropic host) is less than 0.001 GPa. This suggests that it is not necessary in practice to consider the anisotropy of garnet host. This has been also reported in e.g. Mazzucchelli et al. (2019). It was suggested that the elastic anisotropy of cubic garnet has no significant impact on the result of elastic barometry. Thus, effective isotropic elastic properties of garnets may be used to model the inclusion-host elastic interaction.

#### 4. Model applications

##### 4.1 Effect of inclusion aspect ratio on residual stresses

In Eq. 8, the aspect ratio of the inclusion only affects the Eshelby tensor. Here, we choose some common inclusions in metamorphic garnets, including quartz, apatite, zircon and rutile as examples to test the effect of inclusion aspect ratio on residual stresses. The data sources of elastic stiffness tensors of the studied minerals are listed in the caption of Fig. 3. Here, we first focus on spheroidal inclusions, and let the crystallographic  $c$ -axis coincide with the geometrical  $z$ -axis of the inclusion. The inclusion aspect ratio is controlled by varying the lengths of the principal  $z$ - and  $x$ -( $y$ )-axes, and it is denoted by  $c/a$  ratio for simplicity in the following text (note it is not the ratio of the lattice parameters  $c$  and  $a$ ).

To isolate the effect of the inclusion aspect ratio, the eigenstrains for various inclusion minerals are all set to create 1 GPa compressive hydrostatic residual stress for the reference spherical inclusion embedded in an isotropic, infinite garnet host, which is the same approach as in the previous “cross-validation” section. Therefore, the stress variations shown in Fig. 3 only represent the mechanical effect purely due to varying the geometrical aspect ratio  $c/a$ , and they allow direct comparison among different common mineral inclusions in metamorphic garnets.

245 Among all the tested minerals, the residual stress in quartz inclusions is the least sensitive to variations in aspect ratio. For prolate quartz inclusion ( $c/a > 1$ ), the change of  $\sigma_x^{\text{res}}$  due to shape variation is within 0.1 GPa and the change of  $\sigma_z^{\text{res}}$  is within 0.2 GPa. The effects of varying the aspect ratio of prolate zircon and apatite inclusions are similar, with variation of  $\sigma_x^{\text{res}}$  from the reference spherical case reaching up to ca. 0.12 GPa and  $\sigma_z^{\text{res}}$  up to ca. 0.2 GPa.

The residual stress in rutile is the most sensitive to aspect ratio ~~variations~~ variations. With increasing  $c/a$  ratio from 1,  $\sigma_x^{\text{res}}$  in prolate rutile inclusions increases up to ca. 0.2 GPa and  $\sigma_z^{\text{res}}$  decreases by ca. 0.6 GPa. This is relevant for practical measurement as rutile often forms needle-shaped crystals.

250 The pressure (negative mean stress) is significantly less sensitive to inclusion aspect ratio variations. For prolate inclusions of quartz, zircon and apatite, the residual pressure differs from the reference level (spherical inclusion shape) by only ca. 0.01 GPa when the aspect ratio  $c/a$  is stretched up to 4. For oblate inclusion ( $c/a < 1$ ), the pressure variation is typically below 0.1 GPa. An explanation for the stress of rutile being more sensitive to aspect ratio is potentially its high degree of anisotropy. However, care must be taken to interpret the sensitivity of stress to aspect ratio, and individual mineral must be studied individually.

255 The residual stress in mineral inclusions can be easily converted into residual strain, which can be directly translated into Raman shifts (Angel et al., 2019; Murri et al., 2018). The effects of varying the aspect ratio of a quartz inclusion on Raman wavenumber shifts (see Fig. 4) are determined using the calculated residual strain components and the phonon-mode Grüneisen tensor (Murri et al., 2018). The same model settings are applied, with 1 GPa compressive hydrostatic residual stress characterizing the case of a spherical quartz inclusion. It is shown that for prolate inclusions, aspect ratio only introduces minor effects on the Raman shifts. For example, varying the  $c/a$  ratio between 1 and 5 induces a wavenumber variation of less than 0.3  $\text{cm}^{-1}$  for the 464  $\text{cm}^{-1}$  Raman peak. This is in most cases insignificant from the viewpoint of practical Raman measurements because they are typically on the same level or below the detection limit of a standard Raman machine. The  $b/a$  ratio variations are also shown to be insignificant for the spectral shifts, with changes less than 0.2  $\text{cm}^{-1}$  for the 464  $\text{cm}^{-1}$  peak. For oblate inclusion, the impact of inclusion shape is shown to be more significant. For the 464  $\text{cm}^{-1}$  peak, the change of wavenumber shift can reach 0.8  $\text{cm}^{-1}$  for strongly oblate inclusion ( $c/a = 0.25$ ), and it is ca. 0.3-0.4  $\text{cm}^{-1}$  for less oblate inclusion ( $c/a = 0.5$ ).

265 Our results show good consistency with the Raman data reported in Kouketsu et al. (2014), where quartz inclusions with different aspect ratio were measured and no significant variation on spectral shift was found.

270 It is noted here that the applied phonon-mode Grüneisen tensor requires that the symmetry of the inclusion is preserved, i.e.  $a=b$  ( $\epsilon_{xx}^{\text{incl}} = \epsilon_{yy}^{\text{incl}}$ ) (Angel et al., 2019). However, under non-hydrostatic stress where  $\sigma_{xx}^{\text{incl}} \neq \sigma_{yy}^{\text{incl}}$ , the symmetry is broken so that the coefficients of phonon-mode Grüneisen tensor will not be the same. In here, we are only interested in the amount of departure of the Raman shift from spherical to ellipsoidal case for quartz inclusion in garnet system, thus we assume that the phonon-mode Grüneisen tensor is not affected by the symmetry breaking issue. More importantly, the symmetry breaking

issue of the phonon-mode Grüneisen tensor does not affect the derived analytical solution that is not related to the mechanical equilibrium.

#### 275 **4.2 Effect of inclusion crystallographic orientation with respect to long-axis**

In nature, the crystallographic axes of an inclusion are not necessarily aligned parallel to its geometrical axes. In this section, the effect of varying the crystallographic orientation with respect to the geometrical axes on the resulting Raman wavenumber shift is systematically studied using the proposed analytical model. Here, we reorient the crystallographic *c*-axis of a spheroidal quartz inclusion from its long axis (Fig. 5) between 0 (crystallographic *c*-axis parallel to the geometrical long axis) and 90  
280 degrees (*c*-axis perpendicular to the long axis). The same eigenstrain is applied for quartz as from previous section. The elastic stiffness tensor of quartz is from Heyliger et al., (2003) and of isotropic almandine garnet is from Milani et al., (2015). The predicted Raman spectral shifts are calculated based on the phonon-mode Grüneisen tensor calibrated by Murri et al. (2018).

The results are shown in Fig. 5. For an aspect ratio of 2, the 464  $\text{cm}^{-1}$  band varies ca.  $\pm 0.2 \text{ cm}^{-1}$  when the orientation of the crystallographic *c*-axis is varied between the long and the short geometrical axis. The effect of crystallographic orientation (*c*-  
285 axis) on the Raman shifts increases towards higher aspect ratio. For an aspect ratio of 5, the 464  $\text{cm}^{-1}$  band varies ca.  $\pm 0.4 \text{ cm}^{-1}$ . Similarly, for 206 and 128  $\text{cm}^{-1}$  bands, the maximal wavenumber variations compared to the reference case of a spherical inclusion are ca. 0.8 and 0.3  $\text{cm}^{-1}$ , respectively. The results suggest that the crystallographic orientation of a quartz inclusion with respect to its geometrical axes has no significant impact on the predicted Raman spectral shift, as long as the geometrical aspect ratio is not higher than 2-3.

#### 290 **4.3 Effect of faceted inclusion shape**

The analytical solution presented in this study is derived for an ellipsoidal anisotropic inclusion. However, the shape of a natural mineral inclusion may exhibit corners, edges and facets, which results in stress concentration effects and may have an impact on the overall level of the residual stress.

Here, we explore the possibility of using an effective ellipsoid to fit the shape of a faceted inclusion. We use the equivalent  
295 aspect ratio to calculate the residual stress/strain based on the presented analytical solution for ellipsoidal inclusions. Fitting an arbitrary, irregular shape using an ellipsoid in 3D (or an ellipse in 2D) is a common practice in image analysis (Chaudhuri and Samanta, 1991; Li et al., 1999). A pixelated 3D image is used to ~~calculate the second order moment of the object shape to minimize the~~ obtain an effective ellipsoid that minimizes its mismatch ~~between~~ with the 3D irregular inclusion shape ~~and the effective ellipsoid~~. The method allows for obtaining the lengths and orientations of the major, minor and intermediate axes of  
300 the effective ellipsoid (method described in Appendix and a MATLAB code is provided in supplementary data to perform this task).

Similar to previous sections, we use the eigenstrain components that can load the reference spherical inclusion of any given mineral embedded in isotropic almandine garnet host into 1 GPa compressive residual stress. The tested inclusion shapes

305 include: cylinder, tetrahedron, cuboid, octahedron, hexagonal prism, and icosahedron. To vary the aspect ratio, the inclusion shape is stretched in the  $z$ -axis direction, which is parallel to the crystallographic  $c$ -axis as shown in Fig. 6.

We study five inclusion minerals: quartz (elastic tensor from Heyliger et al., 2003), zircon (Bass, 1995), rutile (Wachtman et al., 1962), fluorapatite (Sha et al., 1994), and diamond (Bass, 1995). Almandine garnet is taken as the host grain (Milani et al., 2015). For each FE mesh, the [sizeboundary](#) of the computational box is set more than 10 times the inclusion [sizeradius](#) and adaptive mesh is generated with highest mesh resolution within and close to the inclusion. 10-node tetrahedron elements with  
310 quadratic (second-order) shape (interpolation) functions for the displacement field are used. In total, there are ca. 2 million elements per model (numerical error less than 0.0003 based on benchmark results in Fig. 2).

The results of numerical simulations are shown in Fig. 6. The effective aspect ratio for all different inclusion shapes together with the residual stress components are given in supplementary data. The residual stress in non-ellipsoidal inclusions based on FE model is heterogeneous and we monitor the stress state: 1) at the centroid (shorten as [CT](#)) point (red dots in Fig. 6), 2) as  
315 the volumetric average ([VA](#)) within the entire inclusion (orange dots)

The root mean square deviation (RMSD, [defined as  \$\sqrt{\sum\_{i=1}^N \Delta x\_i^2 / N}\$ , where  \$\Delta x\_i\$  is the deviation between the FE numerical and analytical results,  \$N\$  is the total number of the runs](#)) is calculated by comparing the residual stress from the finite element solutions based on various stress evaluation scheme (CT/VA) and analytical model using the best-fitted effective aspect ratio (Table 1). It is clearly shown that the VA stresses of quartz, zircon, rutile and apatite inclusion are remarkably similar to the  
320 analytical results, with RMSD generally lower than 0.02-0.03 GPa (ca. 2%). From CT to VA, a significant improvement on RMSD of a factor of 2 to 3 is obtained.

The only exception among the studied minerals is diamond, where the RMSD is higher than in the case of other inclusions, which are elastically softer. This is consistent with the high “geometrical correction factor” reported for diamond in Mazzucchelli et al. (2018). However, as an improvement from Mazzucchelli et al. (2018), where the geometrical correction factor must be applied for all inclusion phases to correct the residual stress due to shape effects, we have found that the stress variation due to varying inclusion shape for minerals such as quartz, zircon, apatite and rutile can be satisfactorily approximated by using the proposed approach of the equivalent ellipsoidal inclusion, with RMSD generally lower than 3-4% for most of the studied inclusion shapes. To achieve this improved and satisfactory level of prediction: 1) we have used best-fit ellipsoids to better approximate inclusion shapes, instead of a crude measure of the length/width ratio of e.g. cuboidal or cylindrical  
330 inclusion; 2) we have considered not only the centroid point of the inclusion (which indeed yields a larger RMSD), but also the volumetric average (VA) for the residual stress state sampled during stress measurements, which interestingly provides a significantly better approximation for the residual stress/strain state of the tested mineral inclusions. [We speculate that this is due to the incorporation of the stresses close to the inclusion-host wall that leads to a closer approximation for the residual stress based on effective ellipsoid.](#) This is practical and useful in Raman measurement because it is possible to perform either  
335 1) multiple-point averaging during Raman analysis within the entire inclusion, or 2) defocus the laser beam to take into account

a larger volume for the inclusion strain heterogeneity. For tiny inclusions (size of ca. 1~3  $\mu\text{m}$ ) and for a typical in-plane laser beam diameter of ca. 1~2  $\mu\text{m}$ , the stress/strain averaging is, in fact, implicitly performed during measurements,. Based on FE analysis, it is clearly shown that the volumetrically averaged stress within the inclusion, rather than centroid point measurements, may provide a closer match compared to the stress predicted based on the presented analytical solution developed for the best-fitted ellipsoid. This effect becomes statistically more significant when the faceted inclusion shape and crystallographic orientation are independent as demonstrated in the next section.

#### 4.4 Irregularly faceted shapes and random crystallographic orientation

In nature, the shape of mineral inclusions is not necessarily highly symmetric as treated in the previous section and the crystallographic orientation can be generally random with respect to the principal geometric axes of the inclusion. Here, a MATLAB script is used to generate completely random 3D inclusion shapes by prescribing random vertices (non-coplanar 5 to 24 vertices) and connecting them to form a closed 3D shape. Delaunay triangulation is used to form 3D volumes enclosed by the triangular faces. “*Tetgen*” software is again used to generate unstructured tetrahedron computational meshes fitted to the inclusion surface. The effective aspect ratio (geometrical longest to shortest axis of the best-fitted effective ellipsoid) is controlled to be within 6. In total, we have generated ca. 500 random 3D inclusion shapes and performed finite element simulation for the previously studied set of anisotropic inclusion minerals (quartz, zircon, rutile, apatite and diamond) to calculate the elastic stress field. The generated random shapes are plotted in supplementary data (see the *.gif* animation to illustrate 100 selected examples of 3D inclusion shapes). We further allow the crystallographic *c*-axis to be pointing along the orientation randomly chosen parallel to either the longest, intermediate or shortest geometrical axis (best-fitted using the method of Chaudhuri and Samanta, 1991). The FE results are compared to the analytical results based on the effective ellipsoidal inclusion with the same crystallographic orientation. This Monte-Carlo type FE simulation allows us to investigate how much stress deviation can be generated for irregularly faceted inclusion shapes with random crystallographic orientation, and how accurate the analytical approach based on the best fitted ellipsoid is to describe the residual stress state in an irregularly shaped inclusion, depending on the stress sampling scheme (CT/VA). The results are plotted in Fig. 7 (raw data of FE simulations can be found in supplementary data).

For centroid point (CT), quartz inclusions have the lowest RMSD of ca. 0.03 GPa for all the three normal stress components and diamond inclusions have the highest RMSD of ca. 0.11 GPa. In general, CT stress shows a systematically higher RMSD than VA stresses. When the stress is volumetrically averaged within the inclusion (VA), the RMSD dramatically drops to a nearly perfect match between the FE results for irregularly faceted inclusion and the analytical prediction based on the best fitted ellipsoid. The RMSD of volumetrically averaged residual stresses (VA) of quartz, zircon, rutile and apatite are all lower than ca. 0.02 GPa (2%) and it shows no obvious dependence on the effective aspect ratio even for the extremely elongated or flattened inclusions (see the near-perfect alignment of the orange dots and 1-to-1 ratio line in the middle and bottom panel of Fig. 7).

Thus the volumetric average of the residual stress within the inclusion provides a sufficiently reliable match between the exact results for irregularly shaped inclusions and the approximate predictions based on the analytical solution. This shows that it is possible to approximate the stress/strain state of the inclusion using an effective ellipsoid shape for the tested inclusions including quartz, zircon, rutile and apatite. Only diamond has a notably higher level of RMSD, exhibiting a systematic discrepancy between the exact numerical and approximate analytical results. This indicates that using the proposed equivalent analytical model for diamond inclusion may lead to a potential overestimation of the residual stress by ca. 0.07 GPa (7%). However, this RMSD may still be acceptable as a crude estimate or may serve as an upper limit for elastic thermobarometry.

## 5. Non-linear elasticity at room $T$ The limit of applicability

The provided analytical solution provides precise stress prediction of an anisotropic ellipsoidal inclusion entrapped in infinite isotropic host after exhumation. A violation of the fundamental assumption may lead to errors of the predicted stress and strain. Here, we discuss these limitations in more details.

### 5.1 Non-linear elasticity

The presented model builds on a linear elastic constitutive law at room temperature, i.e.  $\sigma_i^{\text{res}} = C_{ij}^{\text{incl}} \epsilon_j^{\text{res}}$ . This assumption is appropriate when the residual stresses/strains of the inclusion are low, thus the application of a constant anisotropic stiffness tensor  $C_{ij}^{\text{incl}}$  determined at room  $P$ - $T$  conditions introduces no significant errors. For highly stressed mineral inclusions, e.g. inclusions in diamond host from mantle xenoliths where the residual inclusion pressure may reach several GPa, this approximation may lead to non-negligible deviations. To eliminate such error, the stiffness tensor  $C_{ij}^{\text{incl}}$  needs to be treated as a function of either non-hydrostatic stresses or anisotropic strains, i.e.  $C_{ij}^{\text{incl}}(\sigma_i^{\text{res}})$  or  $C_{ij}^{\text{incl}}(\epsilon_i^{\text{res}})$ . In experimental studies,  $C_{ij}^{\text{incl}}$  is often described as a function of hydrostatic pressure, e.g. Bass (1995). It is beyond the scope of this paper to develop a method of fitting  $C_{ij}^{\text{incl}}$  with respect to the individual stress tensor components. If the stiffness tensor  $C_{ij}^{\text{incl}}$  can be parameterized by  $\sigma_i^{\text{res}}$  or simply as a function of pressure as a first-order approximation, the residual stresses/strains are readily calculated by iterating Eq. 8, while updating the  $C_{ij}^{\text{incl}}$  tensor using the calculated inclusion stress or strain during the iteration loop. Thus, the developed analytical method based on the Eshelby's solution can be extended to the case of a non-linear inclusion phase as long as  $C_{ij}^{\text{incl}}$  can be parametrized in terms of stress or strain components, or their invariants.

### 5.2 Irregularity of the inclusion shape

Inclusions are not perfectly ellipsoidal but can be effectively approximated as a smoothed, best-fitted effective ellipsoid. In the above sections (4.3 and 4.4), it has been shown that regardless of the inclusion shape, it is possible to use a best-fitted effective ellipsoid inclusion shape to approximate the actual faceted, irregular inclusion shape. By using such approximate, the predicted stress error is typically within 2%. This requires obtaining the irregular inclusion shape and fit it with an effective ellipsoid (see Appendix for code).

### 5.3 Anisotropy of the host

400 The presented model treats the host as perfectly isotropic. However, even garnet (cubic) host is not perfectly isotropic. It is not straightforward to formulate an explicit analytical form for the residual stress of an anisotropic inclusion in anisotropic host, especially when the principal axes of them do not align. Therefore, we limit ourselves in this work to isotropic host, as e.g. garnet can be approximated as an isotropic material. In Fig. 2, we show that the difference of residual stress of a quartz inclusion in a cubic garnet and isotropic garnet is negligible. However, care must be taken when using other mineral hosts with more anisotropic elasticity, e.g. amphibole, epidote, olivine etc.

### 5.4 Distance to the thin-section surface

405 The presented model takes the assumption that the host is infinite. The issue of proximity of the inclusion to thin-section surface has been discussed in more details in e.g. (Campomenosi et al., 2018; Mazzucchelli et al., 2018; Zhong et al., 2019a, 2020). For typical inclusion-host system, the distance from inclusion center to thin-section surface should be at least 2~3 times the inclusion radius to avoid substantial stress release. As long as this assumption is satisfied, our obtained analytical solution  
410 will not be influenced by this factor.

## **6. Concluding remarks and petrological implications**

In this study, we use the classical Eshelby solution combined with the equivalent eigenstrain method to calculate the residual strain and stress in an anisotropic, ellipsoidal mineral inclusion embedded in an elastically isotropic host. The residual stresses can be expressed by a linear operator (Eq. 8) acting on the eigenstrain. The linear operator depends on the anisotropic elastic stiffness tensor of the inclusion evaluated at room P-T conditions, the shape of the inclusion, and the shear modulus and Poisson ratio of the host. The studied mechanical problem is loaded by an eigenstrain term, which is given by the difference between the lattice strains of the inclusion and host at the P-T conditions of entrapment.

The effect of inclusion aspect ratio on the inclusion residual stress and strain has been investigated quantitatively. The residual stress in quartz inclusions exhibits the least sensitivity to aspect ratio changes and rutile shows the most pronounced variation.

420 ~~The popularly used quartz-in-garnet system is, thus needs to be studied in more details with caution.~~ For prolate quartz inclusions, the residual stress variations caused by varying inclusion shape are shown to be insignificant when the crystallographic *c*-axis is subparallel to the geometrical long axis. The Raman wavenumber variation is less than 0.4 cm<sup>-1</sup> for the 464 cm<sup>-1</sup> peak even for highly elongated inclusions with an aspect ratio of 5. For oblate quartz inclusions with an aspect ratio of ca. 0.5, the additional wavenumber shift may reach ca. 0.8 cm<sup>-1</sup>. ~~Therefore, it is useful in practice, although potentially technically difficult, to have an estimate of the crystallographic *c*-axis orientation when studying highly stretched or flattened quartz inclusions. As~~ Therefore, as long as the *c*-axis is sub-parallel to the geometrical long-axis, the additional wavenumber shifts due to the inclusion aspect ratio is minor.

Our proposed analytical procedures to model residual inclusion stress and strain state do not require pre-FE simulation to obtain the 6-by-6 "relaxation tensor" as proposed by Mazzucchelli et al. (2019). For application purposes, as long as the lattice strains of inclusion ( $\epsilon_i^{\text{incl}}$ ) and host ( $\epsilon_i^{\text{host}}$ ) at high  $P$ - $T$  conditions are available, it is possible to calculate the eigenstrain term by subtracting them following Eq. 2. Given the driving eigenstrain, the residual strain and stress preserved within an anisotropic, ellipsoidal inclusion in isotropic host can be easily calculated using Eq. 8. The proposed procedure can be inversely applied to retrieve the residual strain/stress of any natural mineral inclusions embedded in elastically isotropic hosts, such as garnets.

~~The presented model is only exact for perfectly ellipsoidal inclusions.~~ In nature, inclusions often possess different shapes with facets and edges. Finite element simulations on various faceted inclusion shapes showed that the residual stress is modified to a different degree as compared to the simple ellipsoidal inclusion case, depending on the relative elastic properties between the inclusion and the host grain. ~~However, the~~The proposed approach of using the analytical result for the best-fitted effective ellipsoids yields remarkably good approximation for all the tested inclusion shapes, including highly irregular. The RMSD comparing the FE numerical solution for faceted inclusion and the analytical solution based on effective best-fitted ellipsoid is typically less than 2% for quartz, zircon, apatite and rutile inclusions. The only exception are the elastically stiff diamond inclusions, where the RMSD reaches 7%. This finding expands the applicability of the analytical framework to arbitrarily shaped inclusions, whose elastic stiffness is not ~~significantly~~ significantly higher than host (such as quartz, rutile, zircon and apatite). One important petrological implication is that it is possible to take the volumetrically averaged stress/strain within the inclusion and use it as a proxy to represent the residual stress/strain state of the inclusion. Then the proposed analytical framework may be used to recover the entrapment condition by back-calculating the eigenstrain using the volumetrically averaged residual stress/strain and the effective ellipsoid aspect ratio of the inclusion (Eq. 8). In fact, averaging the stress/strain within a certain volume is implicitly done in practical Raman measurement, for example for tiny  $\mu\text{m}$  size inclusion with laser beam size typically exceeding 1  $\mu\text{m}$ .

#### **Author contribution**

XZ and MD conceived the idea and developed the analytical method. XZ did the Finite Element model. XZ, MD and BJ wrote the manuscript together.

#### **Code availability**

All MATLAB codes have been uploaded as supplementary files. Details to use the code can be found in Appendix or directly contact via xinzhong0708@gmail.com.

#### **Data availability**

All calculated data are available as excel file with details provided in Appendix.

## Acknowledgements and Declarations

This work ~~has been finished during~~ was started in 2017–2018 and the paper has been submitted to American Mineralogist in Nov. 2018 (No. 6895) with two major rounds of reviews but was finally rejected after one year. Later it was submitted to Contributions to Mineralogy and Petrology in late 2019 and Lithos in 2020 with complete revision but was rejected ~~potentially due to conflict of interest~~. We acknowledge the team of reviewers who have commented this manuscript. This project has been supported by the early postdoc mobility fellowship of Swiss National Science Foundation (P2EZZP2\_172220) and the Alexander von Humboldt fellowship to XZ, and the European Union's Horizon 2020 Research and Innovation Programme under the ERC Advanced Grant Agreement n°669972, 'Disequilibrium Metamorphism' ('DIME') to BJ. MD acknowledges the PGI-NRI statutory funds (Project No. 62.9012.2063).

## References

- Abramowitz, M. and Stegun, I. A.: Handbook of Mathematical Functions, Dover Publications., 1964.
- Alvaro, M., Mazzucchelli, M. L., Angel, R. J., Murri, M., Campomenosi, N., Scambelluri, M., Nestola, F., Korsakov, A., Tomilenko, A. A., Marone, F. and Morana, M.: Fossil subduction recorded by quartz from the coesite stability field, *Geology*, 48(1), 24–28, doi:10.1130/G46617.1, 2020.
- [Anderson, G. M.: Error propagation by the Monte Carlo method in geochemical calculations, \*Geochim. Cosmochim. Acta\*, 40\(12\), 1533–1538, doi:10.1016/0016-7037\(76\)90092-2, 1976.](#)
- Angel, R. J., Mazzucchelli, M. L., Alvaro, M. and Nestola, F.: EosFit-Pinc: A simple GUI for host-inclusion elastic thermobarometry, *Am. Mineral.*, 102(9), 1957–1960, doi:10.2138/am-2017-6190, 2017.
- Angel, R. J., Murri, M., Mihailova, B. and Alvaro, M.: Stress, strain and Raman shifts, *Zeitschrift für Krist.*, 234, 129–140, doi:doi.org/10.1515/zkri-2018-2112, 2019.
- Ashley, K. T., Caddick, M. J., Steele-MacInnis, M. J., Bodnar, R. J. and Dragovic, B.: Geothermobarometric history of subduction recorded by quartz inclusions in garnet, *Geochemistry, Geophys. Geosystems*, 15(2), 350–360, doi:10.1002/2013GC005106, 2014.
- Bass, J. D.: Elasticity of Minerals, Glasses, and Melts, in *Mineral Physics & Crystallography: A Handbook of Physical Constants*, pp. 45–63., 1995.
- Bayet, L., John, T., Agard, P., Gao, J. and Li, J.: Massive sediment accretion at ~ 80 km depth along the subduction interface : Evidence from the southern Chinese Tianshan, *Geology*, 46(6), 495–498, 2018.
- Bonaccorso, A. and Davis, P. M.: Models of ground deformation from vertical volcanic conduits with application to eruptions of Mount St. Helens and Mount Etna, *J. Geophys. Res. Solid Earth*, 104(B5), 10531–10542, doi:10.1029/1999jb900054, 1999.

Bonazzi, M., Tumiati, S., Thomas, J., Angel, R. J. and Alvaro, M.: Assessment of the reliability of elastic geobarometry with quartz inclusions, *Lithos*, 350–351, 105201, doi:10.1016/j.lithos.2019.105201, 2019.

[Briggs, R. J. and Ramdas, A. K.: Piezospectroscopy of the Raman spectrum of alpha-quartz, \*Phys. Rev. B\*, 16, 1977.](#)

490 [Campomenosi, N., Mazzucchelli, M. L., Mihailova, B. D., Scambelluri, M., Angel, R. J., Nestola, F., Reali, A. and Alvaro, M.: How geometry and anisotropy affect residual strain in host inclusion system: coupling experimental and numerical approaches, \*Am. Mineral.\*, 103, 2032–2035, doi:10.1111/ijlh.12426, 2018.](#)

Chaudhuri, B. B. and Samanta, G. P.: Elliptic fit of objects in two and three dimensions by moment of inertia optimization, *Pattern Recognit. Lett.*, 12(1), 1–7, doi:10.1016/0167-8655(91)90021-D, 1991.

495 [Chiu, Y. P.: On the Stress Field and Surface Deformation in a Half Space With a Cuboidal Zone in Which Initial Strains Are Uniform, \*J. Appl. Mech.\*, 45\(2\), 302, doi:10.1115/1.3424292, 1978.](#)

Cliffe, M. J. and Goodwin, A. L.: PASCAL: A principal axis strain calculator for thermal expansion and compressibility determination, *J. Appl. Crystallogr.*, 45(6), 1321–1329, doi:10.1107/S0021889812043026, 2012.

500 [Dabrowski, M., Krotkiewski, M. and Schmid, D. W.: MILAMIN: MATLAB-based finite element method solver for large problems, \*Geochemistry, Geophys. Geosystems\*, 9\(4\), 1–24, doi:10.1029/2007GC001719, 2008.](#)

Enami, M., Nishiyama, T. and Mouri, T.: Laser Raman microspectrometry of metamorphic quartz: A simple method for comparison of metamorphic pressures, *Am. Mineral.*, 92(8–9), 1303–1315, doi:10.2138/am.2007.2438, 2007.

505 [Eshelby, J. D.: The determination of the elastic field of an ellipsoidal inclusion, and related problems, in \*Proceedings of the Royal Society of London A: Mathematical, Physical and Engineering Sciences\*, vol. 241, pp. 376–396, The Royal Society., 1957.](#)

Exner, U. and Dabrowski, M.: Monoclinic and triclinic 3D flanking structures around elliptical cracks, *J. Struct. Geol.*, 32(12), 2009–2021, doi:10.1016/j.jsg.2010.08.002, 2010.

Freeman, B.: The behaviour of deformable ellipsoidal particles in three-dimensional slow flows: implications for geological strain analysis, *Tectonophysics*, 132(4), 297–309, doi:10.1016/0040-1951(87)90349-0, 1987.

510 [Ghosh, S. and Dimiduk, D.: Computational methods for microstructure-property relationships., 2011.](#)

Gillet, P., Ingrin, J. and Chopin, C.: Coesite in subducted continental crust : P - T history deduced from an elastic model, *Earth Planet. Sci. Lett.*, 70, 426–436, 1984.

515 [Gonzalez, J. P., Thomas, J. B., Baldwin, S. L. and Alvaro, M.: Quartz-in-garnet and Ti-in-quartz thermobarometry: Methodology and first application to a quartzofeldspathic gneiss from eastern Papua New Guinea, \*J. Metamorph. Geol.\*, 37\(9\), 1193–1208, doi:10.1111/jmg.12508, 2019.](#)

Guiraud, M. and Powell, R.: P-V-T relationships and mineral equilibria in inclusions in minerals, *Earth Planet. Sci. Lett.*, 244, 683–694, doi:10.1016/j.epsl.2006.02.021, 2006.

Healy, D., Jones, R. R. and Holdsworth, R. E.: Three-dimensional brittle shear fracturing by tensile crack interaction, *Nature*, 439(7072), 64–67, doi:10.1038/nature04346, 2006.

520 Heyliger, P., Ledbetter, H. and Kim, S.: Elastic constants of natural quartz., *J. Acoust. Soc. Am.*, 114(2), 644–650, doi:10.1121/1.1593063, 2003.

Jiang, D.: Viscous inclusions in anisotropic materials: Theoretical development and perspective applications, *Tectonophysics*, 693(October 2016), 116–142, doi:10.1016/j.tecto.2016.10.012, 2016.

Jiang, F., Speziale, S. and Duffy, T. S.: Single-crystal elasticity of grossular- and almandine-rich garnets to 11 GPa by Brillouin scattering, *J. Geophys. Res.*, 109, B10210, doi:10.1029/2004JB003081, 2004.

525 Kouketsu, Y., Nishiyama, T., Ikeda, T. and Eniami, M.: Evaluation of residual pressure in an inclusion – host system using negative frequency shift of quartz Raman spectra, *Am. Mineral.*, 99(2000), 433–442, 2014.

Li, M., Ghosh, S., Richmond, O., Weiland, H. and Rouns, T. N.: Three dimensional characterization and modeling of particle reinforced metal matrix composites: Part I: Quantitative description of microstructural morphology, *Mater. Sci. Eng. A*, 265(1–2), 153–173, doi:10.1016/S0921-5093(98)01132-0, 1999.

530 Mazzucchelli, M. L., Burnley, P., Angel, R. J., Morganti, S., Domeneghetti, M. C., Nestola, F. and Alvaro, M.: Elastic geothermobarometry: Corrections for the geometry of the host-inclusion system, *Geology*, 46(3), 1–4, doi:10.1130/G39807.1, 2018.

Mazzucchelli, M. L., Reali, A., Morganti, S., Angel, R. J. and Alvaro, M.: Elastic geobarometry for anisotropic inclusions in cubic hosts, *Lithos*, 350–351, 105218, doi:10.1016/j.lithos.2019.105218, 2019.

Meng, C. and Pollard, D. D.: Eshelby’s solution for ellipsoidal inhomogeneous inclusions with applications to compaction bands, *J. Struct. Geol.*, 67(PA), 1–19, doi:10.1016/j.jsg.2014.07.002, 2014.

Milani, S., Nestola, F., Alvaro, M., Pasqual, D., Mazzucchelli, M. L., Domeneghetti, M. C. and Geiger, C. A.: Diamond-garnet geobarometry: The role of garnet compressibility and expansivity, *Lithos*, 227, 140–147, doi:10.1016/j.lithos.2015.03.017, 2015.

540 Morganti, S., Mazzucchelli, M. L., Alvaro, M. and Reali, A.: A numerical application of the Eshelby theory for geobarometry of non-ideal host-inclusion systems, *Meccanica*, 55(4), 751–764, doi:10.1007/s11012-020-01135-z, 2020.

Mura, T.: *Micromechanics of Defects in Solids*, Springer Science & Business Media., 1987.

- Murri, M., Mazzucchelli, M. L., Campomenosi, N., Korsakov, A. V., Prencipe, M., Mihailova, B. D., Scambelluri, M.,  
545 Angel, R. J. and Alvaro, M.: Raman elastic geobarometry for anisotropic mineral inclusions, *Am. Mineral.*, 113, 1869–1872,  
2018.
- Ohashi, Y. and Burnham, C. W.: Clinopyroxene Lattice Deformations: The Roles of Chemical Substitution and  
Temperature, *Am. Mineral.*, 58, 843–849, 1973.
- Rosenfeld, J. L. and Chase, A. B.: Pressure and temperature of crystallization from elastic effects around solid inclusions in  
550 minerals?, *Am. J. Sci.*, 259, 519–541, doi:10.2475/ajs.259.7.519, 1961.
- Sha, M. C., Li, Z. and Bradt, R. C.: Single-crystal elastic constants of fluorapatite, Ca<sub>5</sub>F(PO<sub>4</sub>)<sub>3</sub>, *J. Appl. Phys.*, 75(12),  
7784–7787, doi:10.1063/1.357030, 1994.
- Si, H.: TetGen, a Quality Tetrahedral Mesh Generator, *AMC Trans. Math. Softw.*, 41(2), 11, doi:10.1007/3-540-29090-7\_9,  
2015.
- 555 Taguchi, T., Enami, M. and Kouketsu, Y.: Prograde evolution of Sulu UHP metamorphic rock in Yangzhuang, Junan region,  
deduced by combined Raman and petrological studies, *J. Metamorph. Geol.*, 34(7), 683–696, doi:10.1111/jmg.12203, 2016.
- Taguchi, T., Enami, M. and Kouketsu, Y.: Metamorphic record of the Asemi-gawa eclogite unit in the Sanbagawa belt,  
southwest Japan: Constraints from inclusions study in garnet porphyroblasts, *J. Metamorph. Geol.*, 37(2), 181–201,  
doi:10.1111/jmg.12456, 2019.
- 560 Thomas, J. B. and Spear, F. S.: Experimental study of quartz inclusions in garnet at pressures up to 3.0 GPa: evaluating  
validity of the quartz-in-garnet inclusion elastic thermobarometer, *Contrib. Mineral. Petrol.*, 173(5), 1–14,  
doi:10.1007/s00410-018-1469-y, 2018.
- Voigt, W.: *Lehrbuch der kristallphysik*, B. G. Teubner. Berlin., 1910.
- Wachtman, J. B., Tefft, W. E. and Lam, D. G.: Elastic constants of rutile (TiO<sub>2</sub>), *J. Res. Natl. Bur. Stand. Sect. A Phys.*  
565 *Chem.*, 66A(6), 465, doi:10.6028/jres.066a.047, 1962.
- Zhang, Y.: Mechanical and phase equilibria in inclusion-host systems, *Earth Planet. Sci. Lett.*, 157(3–4), 209–222,  
doi:10.1016/S0012-821X(98)00036-3, 1998.
- Zhong, X., Dabrowski, M. and Jamtveit, B.: Analytical solution for the stress field in elastic half-space with a spherical  
pressurized cavity or inclusion containing eigenstrain, *Geophys. J. Int.*, 216, ~~1100–1115~~, 2018(2), doi:10.1093/gji/gy447,  
570 [2019a](#).
- Zhong, X., Andersen, N. H., Dabrowski, M. and Jamtveit, B.: Zircon and quartz inclusions in garnet used for complimentary  
Raman- thermobarometry: application to the Holsnøy eclogite, Bergen Arcs, Western Norway, *Contrib. Mineral. Petrol.*, 4,  
1–17, doi:10.1007/s00410-019-1584-4, [20192019b](#).

575 [Zhong, X., Moulas, E. and Tajčmanová, L.: Post-entrapment modification of residual inclusion pressure and its implications for Raman elastic thermobarometry, \*Solid Earth\*, 11\(1\), 223–240, doi:10.5194/se-11-223-2020, 2020.](#)

## Figures and Tables

580 **Table 1.** Root mean square deviation (RMSD) of finite element solution of symmetrically shaped non-ellipsoidal inclusion in  
 Fig. 6 compared to the analytical solution of equivalent spheroidal inclusions. Isotropic almandine garnet is used as host. For  
 each inclusion mineral and inclusion shape, the aspect ratio varies from 0.2~5. Effective aspect ratio is calculated for each  
 shape and used for the analytical solution to obtain the residual stress state. The inclusion is loaded by eigenstrain that creates  
 1 GPa hydrostatic residual pressure for spherical inclusion in infinite host. Thus, any stress variation can only be caused by  
 585 shape change. The calculated stress data for each individual FE run is given in supplementary data. Stress is obtained for 1)  
 the centroid point (CT), and 2) volumetric average (VA) of the entire inclusion (see Fig. 6 for illustration). The RMSD is  
 calculated by comparing the FE results and analytical results based on the best-fitted effective ellipsoid. The unit of RMSD is  
 in GPa. Elasticity of inclusion mineral given in the caption of Fig. 6.

Shape	Cylinder		Tetrahedron		Cuboid		Hexagonal		Octahedron		Icosahedron	
Location	CT	VA	CT	VA	CT	VA	CT	VA	CT	VA	CT	VA
Quartz	0.041	0.021	0.034	0.044	0.042	0.026	0.038	0.021	0.055	0.022	0.011	0.005
Zircon	0.045	0.023	0.042	0.048	0.112	0.028	0.047	0.024	0.084	0.017	0.028	0.006
Rutile	0.063	0.039	0.049	0.029	0.158	0.039	0.065	0.039	0.127	0.026	0.034	0.003
Apatite	0.047	0.029	0.052	0.057	0.049	0.035	0.045	0.029	0.062	0.024	0.014	0.007
Diamond	0.136	0.071	0.191	0.255	0.171	0.095	0.136	0.081	0.079	0.125	0.022	0.027

Formatted Table

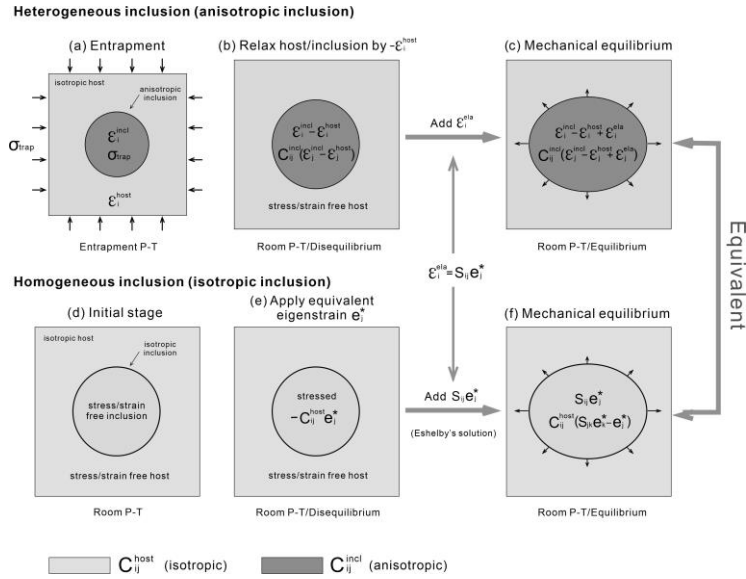


**Fig. 1.** Schematic diagram showing how to obtain the residual stress/strain of anisotropic inclusion in isotropic host. (a) Inclusion-host at entrapment conditions. The stress is homogeneous as  $\sigma_{\text{trap}}$  but strains are different as  $\epsilon_i^{\text{incl}}$  and  $\epsilon_i^{\text{host}}$ . (b) First, relax the inclusion and host by  $-\epsilon_i^{\text{host}}$  to room  $P$ - $T$  conditions. Without elastic interaction, the inclusion has strain  $\epsilon_i^{\text{incl}}$  and stress  $C_{ij}^{\text{incl}}(\epsilon_i^{\text{incl}} - \epsilon_i^{\text{host}})$  so the system is not in mechanical equilibrium. (c) Elastic interaction occurs to reach equilibrium by adding strain  $\epsilon_i$  to the inclusion (host also deforms). The residual inclusion stress is  $C_{ij}^{\text{incl}}(\epsilon_i^{\text{incl}} - \epsilon_i^{\text{host}} + \epsilon_i)$ . (d) Equivalent scenario where the inclusion and host are initially stress free at room  $P$ - $T$  and they both have isotropic elasticity of  $C_{ij}^{\text{host}}$ . (e) Equivalent eigenstrains  $e_i^*$  are loaded to the inclusion. Without elastic interaction, the inclusion has stress  $-C_{ij}^{\text{incl}} e_j^*$ . Eshelby's method is applied to obtain the final strain state in isotropic inclusion as  $S_{ij} e_j^*$  and stress as  $C_{ij}^{\text{incl}}(S_{jk} e_k^* - e_j^*)$ , where  $S_{ij}$  is the Eshelby's tensor (Eshelby, 1957). Equivalent eigenstrain method states that by properly choosing  $e_i^*$ , the relation  $\epsilon_i = S_{ij} e_j^*$  can be satisfied (Mura, 1987, chapter 4). The stress of isotropic inclusion (f) as  $C_{ij}^{\text{host}}(S_{jk} e_k^* - e_j^*)$  equals the stress of the anisotropic inclusion (c) as  $C_{ij}^{\text{incl}}(\epsilon_j^{\text{incl}} - \epsilon_j^{\text{host}} + S_{jk} e_k^*)$  (see Eq. 7). By solving for  $e_j^*$ , we obtain the residual stress and strain of anisotropic inclusion in isotropic host in Eq. 8.

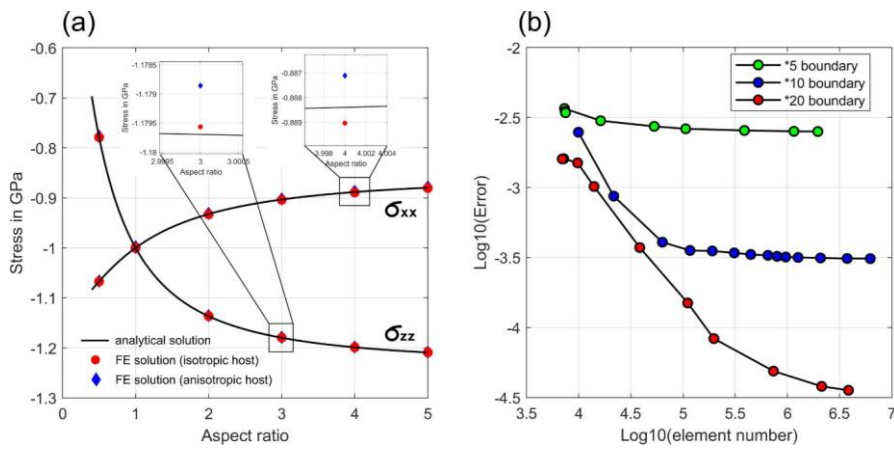
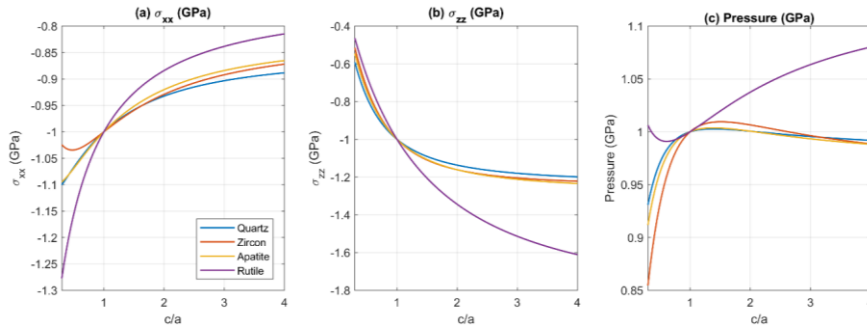


**Fig. 2.** Cross validation results between finite element method and the presented analytical method. (a) Direct comparison of residual stress components calculated with FE method and analytical method as a function of the aspect ratio of a spheroidal inclusion. (b) The normalized unsigned difference of the stress between FE method and analytical method as a function of mesh element number and model domain size. Spherical inclusion is used and boundary distance is set to \*5, \*10 and \*20 the inclusion diameter.



615 **Fig. 3.** Effect of geometrical aspect ratio of spheroidal inclusion along  $c$  and  $a$ -axes on residual stress ( $c/a$ ). (a-b) Stresses  $\sigma_{xx}^{\text{res}}$   
and  $\sigma_{zz}^{\text{res}}$  as a function of the geometrical  $c/a$  ratio for quartz, zircon, apatite and rutile inclusions. To isolate the effects of  
aspect ratio, the eigenstrain are set to produce  $\sigma_{xx}^{\text{res}} = \sigma_{zz}^{\text{res}} = -1$  GPa for the reference spherical inclusion. Any deviation from  
-1 GPa is due to shape changes. (c) Pressure as a function of the  $c/a$  ratio. Here, the crystallographic  $c$ -axes isare aligned  
parallel to the long axis for prolate inclusions and short axis for oblate inclusions. The quartz elastic stiffness tensor is from  
620 Heyliger et al., (2003); zircon and diamond from Bass, (1995); rutile from Wachtman et al. (1962); apatite from Sha et al.  
(1994). Isotropic stiffness tensor of almandine host is from Milani et al. (2015).

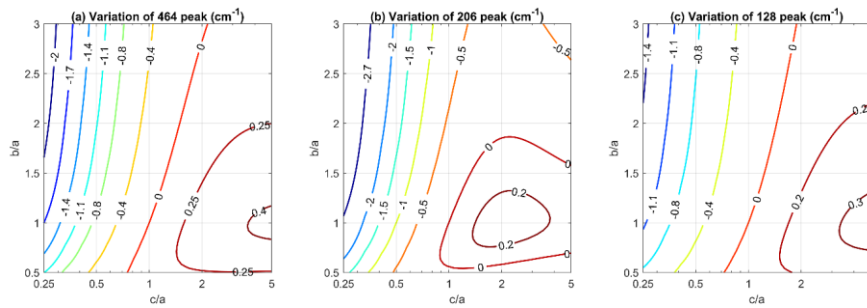


**Fig. 4.** The effect of geometrical aspect ratio of ellipsoidal quartz inclusion for  $c/a$ -axes and  $b/a$ -axes on Raman wavenumber shift entrapped in [almandine](#) garnet host. The contours show the variation of wavenumber shift compared to perfectly spherical quartz inclusion ( $c/a=1$ ,  $b/a=1$ ). The initial residual inclusion pressure is assumed to be hydrostatic 1 GPa for the reference spherical inclusion. The wavenumber shift variation are due to changing the geometrical aspect ratios of  $c/a$  and  $b/a$  axes. The Raman shifts are calculated using the residual strain and the [phonon-mode](#) Grüneisen tensor in Murri et al. (2018). For  $c/a > 1$ , the inclusion is prolate and for  $c/a < 1$ , the inclusion is oblate. The stiffness tensor of quartz at room  $P$ - $T$  is from Heyliger et al., (2003) and almandine garnet from Milani et al. (2015).

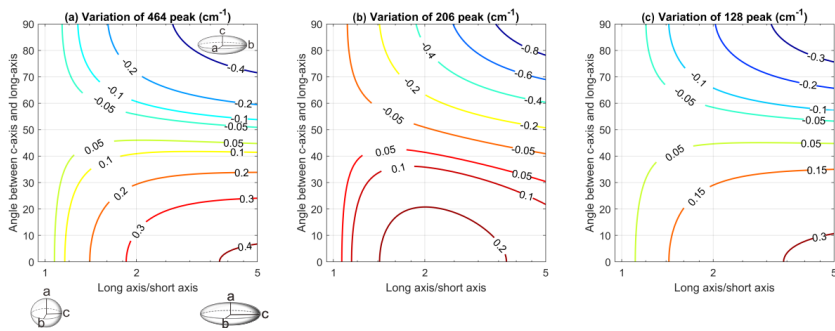


**Fig. 5.** The effect of varying the crystallographic orientation (*c*-axis) with respect to the geometrical long axis of a prolate spheroidal quartz inclusion. The contours show the variation of wavenumber shift compared to perfectly spherical quartz inclusion  $c/a=1$  (in this case the crystallographic orientation does not matter). The horizontal axis represents the aspect ratio of the spheroidal inclusion, and the vertical axis shows the angle between the crystallographic *c*-axis and the geometrical long axis. In the plot, *c*-axis is allowed to shift from parallel to the geometrical long axis to parallel to geometrical short axis of the spheroidal inclusion. The driving eigenstrain is set to produce a hydrostatic residual pressure of 1 GPa in the reference spherical inclusion.

635

640

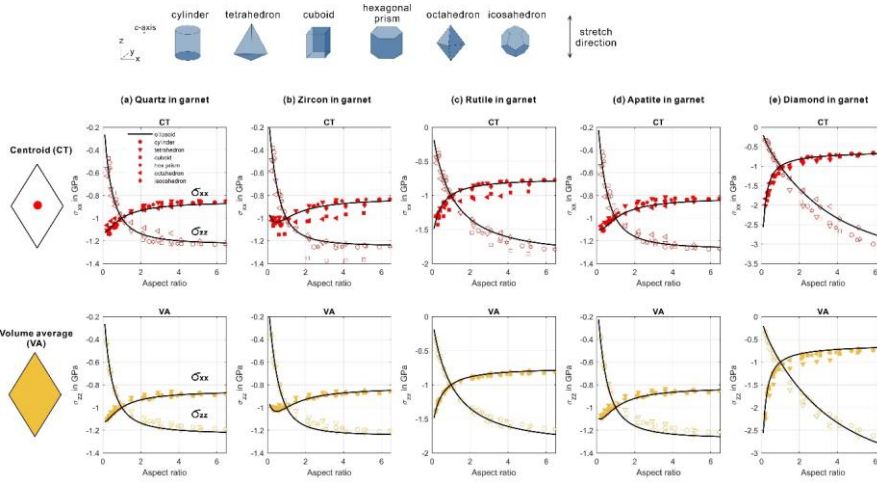


**Fig. 6.** Finite element stress of various inclusion shapes (symbols) compared to the stress of effective spheroidal inclusion based on analytical method (black curves). The effective aspect ratio of inclusion shape is calculated based on the fitting method of Chaudhuri and Samanta, (1991) and Li et al. (1999) (see Appendix). The inclusion is loaded with eigenstrain that generates 1 GPa compressive hydrostatic residual stress for spherical shape. The variation of stress is only caused by the shape change. The  $c$ -axis coincides with the stretching direction. The red dots correspond to the stress at the inclusion's centroid (CT), the orange dots correspond to the volumetric average (VA) of the entire inclusion. The anisotropic elastic stiffness tensor are listed in the caption of Fig. 3. The root mean square deviation (RMSD) for each inclusion shape and inclusion mineral phase is given in Table 1. The raw FE stress data can be found in supplementary excel file.

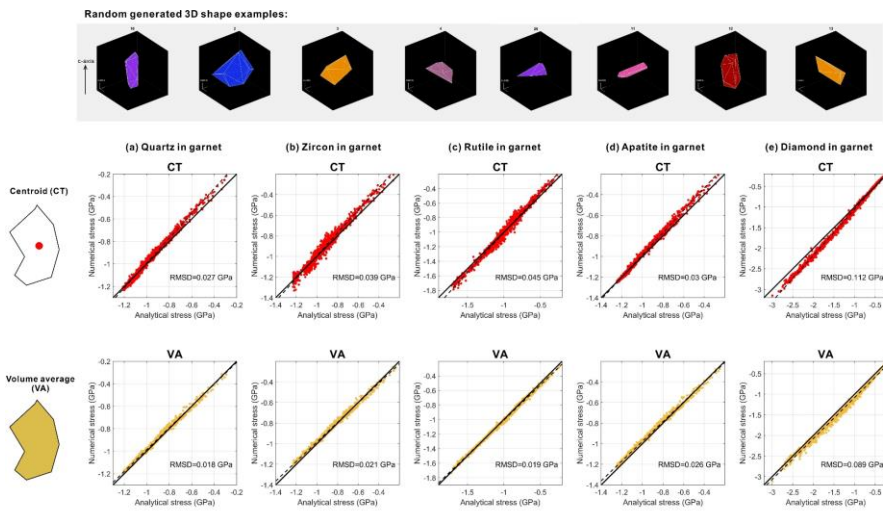


**Fig. 7.** Randomly generated 500 inclusion shapes (top panel for examples) calculated with finite element method (vertical axis) and analytical method (horizontal axis). All three normal stress components are plotted together in each diagram. The crystallographic *c*-axis's orientation is randomly chosen along one of the geometrical principal axes. The red and orange dots show the comparison of FE (numerical) results and analytical results for the normal stress components. Each dot represents a normal stress component calculated for one randomly generated inclusion shape. The red dots show the stress evaluated at the centroid point (CT), the orange dots show the volumetrically averaged (VA) stress within the inclusion. The raw data can be found in supplementary excel file and the generated 3D random shape can be viewed in the .gif file.

655

660 **Appendix**

**Calculate lattice strain at entrapment conditions**

When the inclusion and host crystalized at entrapment conditions, they are considered to be stressed and strained by taking room  $P$ - $T$  condition as the reference state. Therefore, it is possible to calculate their strain state using lattice parameters  $a$ ,  $b$  and  $c$  relative to the reference state  $a_0$ ,  $b_0$   $c_0$ . For cubic, tetragonal and orthorhombic symmetry systems (or hexagonal and trigonal minerals with symmetry being imposed), the lattice strains can be easily expressed following Eq. 1. For triclinic and monoclinic symmetry systems, the basis vectors of unit cell are not all parallel to the Cartesian coordinates  $x$ ,  $y$  and  $z$ . To obtain the lattice strain, we need to transform the coordinate from  $a$ ,  $b$  and  $c$  into  $x$ ,  $y$  and  $z$ . We follow the method from Ohashi and Burnham (1973) to calculate the strain components based on the lattice parameters. Here, a short description on the involved equations is given and detailed can be found the appendix of Ohashi and Burnham (1973). This transformation considers the crystallographic  $c$ -axis parallel to the Cartesian  $z$ -axis and crystallographic  $a^*$ -axis parallel to the Cartesian  $x$ -axis.

The matrix  $Q_0$  that relates the basis vectors of undeformed crystallographic  $a_0$ ,  $b_0$  and  $c_0$ -axes at reference room  $P$ - $T$  conditions to Cartesian coordinates is as follows:

$$Q_0 = \begin{bmatrix} \frac{a_0 p_0}{\sin(\alpha_0)} & \frac{a_0(\cos(\gamma_0) - \cos(\alpha_0)\cos(\beta_0))}{\sin(\alpha_0)} & a_0 \cos(\beta_0) \\ 0 & b_0 \sin(\alpha_0) & b_0 \cos(\alpha_0) \\ 0 & 0 & c_0 \end{bmatrix} \quad (A1)$$

$$p_0 = [1 - \cos^2(\alpha_0) - \cos^2(\beta_0) - \cos^2(\gamma_0) + 2 \cos(\alpha_0) \cos(\beta_0) \cos(\gamma_0)]^{1/2}$$

To obtain the similar transformation matrix relating the deformed crystallographic axes at entrapment conditions to Cartesian coordinates can be easily done by replacing  $a_0$ ,  $b_0$   $c_0$ ,  $\alpha_0$ ,  $\beta_0$ ,  $\gamma_0$  measured at reference  $P$ - $T$  state to  $a$ ,  $b$ ,  $c$ ,  $\alpha$ ,  $\beta$ ,  $\gamma$  that are measured at entrapment condition from Eq. A1. This transformation matrix is denoted as  $Q_1$ . We then calculate the displacement gradient tensor  $E$ :

$$E = Q_0^{-1} Q_1 - I \quad (A2)$$

where  $I$  is the identity matrix. Without considering the antisymmetric rotation tensor, the infinitesimal Lagrangian strain tensor can be expressed as follows:

$$\varepsilon = (E' + E)/2 \quad (A3)$$

A MATLAB code is provided to perform this calculation (*Calculate\_Strain.m*). The input values are the reference lattice parameters measured at room  $P$ - $T$  conditions and the deformed lattice parameters at the entrapment conditions. The outputs are both the infinitesimal and finite Lagrangian strain tensor reported in MATLAB commend window. The results are

Formatted Table

Formatted Table

Formatted Table

numerically the same compared to the available computer programs such as “STRAIN” program that can be found at website: <https://www.cryst.ehu.es/cryst/strain.html>, or “Win\_Strain” program at the website: [http://www.rossangel.com/text\\_strain.htm](http://www.rossangel.com/text_strain.htm).

### 685 Calculate Eshelby’s tensor

The components of Eshelby’s tensor  $S_{ij}$  are expressed as functions of the inclusion’s principal axes length and the Poisson ratio of the isotropic host  $\nu$  (Mura, 1987). A MATLAB script is provided to calculate the Eshelby’s tensor (see more details in the following sections for supplementary data).

$$\begin{aligned}
 S_{11} &= \frac{3a_1^2}{8\pi(1-\nu)} I_{11} + \frac{1-2\nu}{8\pi(1-\nu)} I_1 \\
 S_{22} &= \frac{3a_2^2}{8\pi(1-\nu)} I_{22} + \frac{1-2\nu}{8\pi(1-\nu)} I_2 \\
 S_{33} &= \frac{3a_3^2}{8\pi(1-\nu)} I_{33} + \frac{1-2\nu}{8\pi(1-\nu)} I_3 \\
 S_{12} &= \frac{a_2^2}{8\pi(1-\nu)} I_{12} - \frac{1-2\nu}{8\pi(1-\nu)} I_1 \\
 S_{21} &= \frac{a_1^2}{8\pi(1-\nu)} I_{12} - \frac{1-2\nu}{8\pi(1-\nu)} I_2 \\
 S_{13} &= \frac{a_3^2}{8\pi(1-\nu)} I_{13} - \frac{1-2\nu}{8\pi(1-\nu)} I_1 \\
 S_{31} &= \frac{a_1^2}{8\pi(1-\nu)} I_{13} - \frac{1-2\nu}{8\pi(1-\nu)} I_3 \\
 S_{23} &= \frac{a_2^2}{8\pi(1-\nu)} I_{23} - \frac{1-2\nu}{8\pi(1-\nu)} I_2 \\
 S_{32} &= \frac{a_3^2}{8\pi(1-\nu)} I_{23} - \frac{1-2\nu}{8\pi(1-\nu)} I_3 \\
 S_{44} &= \frac{a_2^2 - a_3^2}{16\pi(1-\nu)} I_{23} + \frac{1-2\nu}{16\pi(1-\nu)} (I_2 + I_3) \\
 S_{55} &= \frac{a_1^2 - a_3^2}{16\pi(1-\nu)} I_{13} + \frac{1-2\nu}{16\pi(1-\nu)} (I_1 + I_3) \\
 S_{66} &= \frac{a_1^2 - a_2^2}{16\pi(1-\nu)} I_{12} + \frac{1-2\nu}{16\pi(1-\nu)} (I_1 + I_2)
 \end{aligned}
 \tag{A4}$$

Formatted Table

690 where  $a_1$ ,  $a_2$  and  $a_3$  are the lengths of three principal axes of the inclusions and they follow the order of  $a_1 > a_2 > a_3$ . In case this order needs to be changes, a simple 90 degree rotation can be executed on  $S_{ij}$ . The provided code in supplementary data automatically perform such rotation to adjust the axes into correct order. The required tensors  $I_i$  and  $I_{ij}$  are evaluated as follows:

$$\begin{aligned}
 I_1 &= \frac{4\pi a_1 a_2 a_3}{(a_1^2 - a_2^2)(a_1^2 - a_3^2)^{1/2}} [F(\theta, k) - E(\theta, k)] \\
 I_3 &= \frac{4\pi a_1 a_2 a_3}{(a_2^2 - a_3^2)(a_1^2 - a_3^2)^{1/2}} \left[ \frac{a_2(a_1^2 - a_3^2)^{1/2}}{a_1 a_3} - E(\theta, k) \right] \\
 I_2 &= 4\pi - I_1 - I_3 \\
 I_{12} &= \frac{I_2 - I_1}{a_1^2 - a_2^2} \\
 I_{13} &= \frac{I_3 - I_1}{a_1^2 - a_3^2} \\
 I_{23} &= \frac{I_3 - I_2}{a_2^2 - a_3^2} \\
 I_{11} &= \frac{1}{3} \left( \frac{4\pi}{a_1^2} - I_{12} - I_{13} \right) \\
 I_{22} &= \frac{1}{3} \left( \frac{4\pi}{a_2^2} - I_{12} - I_{23} \right) \\
 I_{33} &= \frac{1}{3} \left( \frac{4\pi}{a_3^2} - I_{13} - I_{23} \right)
 \end{aligned} \tag{A5}$$

where the functions  $F(\theta, k)$  and  $E(\theta, k)$  denote the incomplete elliptic integrals of the first and second kind:

$$\begin{aligned}
 F(\theta, k) &= \int_0^\theta \frac{dw}{\sqrt{1 - k^2 \sin^2(w)}} \\
 E(\theta, k) &= \int_0^\theta \sqrt{1 - k^2 \sin^2(w)} dw \\
 \theta &= \arcsin\left(\sqrt{1 - \frac{a_3^2}{a_1^2}}\right) \\
 k &= \sqrt{(a_1^2 - a_2^2)/(a_1^2 - a_3^2)}
 \end{aligned} \tag{A6}$$

The integrals  $F(\theta, k)$  and  $E(\theta, k)$  are evaluated using the method of the arithmetic-geometric mean (Abramowitz and Stegenm, 1964, chapter 17). Once  $F(\theta, k)$  and  $E(\theta, k)$  are obtained,  $I$  can be computed and substituted into the Eshelby's tensor.

### Fit arbitrary inclusion shape with effective ellipsoid

The method (details see Chaudhuri and Samanta, 1991; Li et al., 1999) requires a 3D data/image of the inclusion consist of regular cubic voxels, which has volume  $\Delta$  in each voxel and coordinate  $x, y, z$  at the center of each voxel. The inclusion is denoted as domain  $R$ . Its second-order moment matrix is calculated as follows:

$$\begin{aligned}
 I_x &= \iiint_R (y^2 + z^2) dx dy dz \approx \sum_{i=1}^n (y_i^2 + z_i^2) \Delta \\
 I_y &= \iiint_R (x^2 + z^2) dx dy dz \approx \sum_{i=1}^n (x_i^2 + z_i^2) \Delta \\
 I_z &= \iiint_R (x^2 + y^2) dx dy dz \approx \sum_{i=1}^n (x_i^2 + y_i^2) \Delta \\
 I_{xy} &= \iiint_R (-xy) dx dy dz \approx \sum_{i=1}^n (-x_i y_i) \Delta \\
 I_{yz} &= \iiint_R (-yz) dx dy dz \approx \sum_{i=1}^n (-y_i z_i) \Delta \\
 I_{xz} &= \iiint_R (-xz) dx dy dz \approx \sum_{i=1}^n (-x_i z_i) \Delta
 \end{aligned} \tag{A7}$$

700 where  $x_i$  is the  $x$  coordinate of the  $i$  th voxel that makes the inclusion,  $n$  is the total number of the voxels that makes the inclusion domain  $R$ . A symmetric 3-by-3 matrix is constructed with the above six components and its eigenvalues are denoted as  $I_1, I_2$  and  $I_3$ . The length of major, intermediate and minor axes can be calculated straightforwardly as follows, respectively:

$$\begin{aligned}
 a &= \sqrt{\frac{5}{2I_0} (I_2 + I_3 - I_1)} \\
 b &= \sqrt{\frac{5}{2I_0} (I_1 + I_3 - I_2)} \\
 c &= \sqrt{\frac{5}{2I_0} (I_1 + I_2 - I_3)}
 \end{aligned} \tag{A8}$$

705 where  $I_0$  is the volume of the shape  $R$ , which can be straightforwardly calculated as  $I_0 = n\Delta$ . The orientation of the inclusion's maximal principle axes expressed in direction cosine ( $\alpha, \beta$  and  $\gamma$ ) is obtained by minimizing the following equation as a function of direction cosine  $\alpha, \beta$  and  $\gamma$  (done in MATLAB with the constrained minimization "*fmincon*" function):

$$F = [\cos(\alpha), \cos(\beta), \cos(\gamma)] \begin{bmatrix} I_x & I_{xy} & I_{xz} \\ I_{xy} & I_y & I_{yz} \\ I_{xz} & I_{yz} & I_z \end{bmatrix} \begin{bmatrix} \cos(\alpha) \\ \cos(\beta) \\ \cos(\gamma) \end{bmatrix} \tag{A9}$$

where the direction cosine must also satisfy the relation:  $\cos(\alpha)^2 + \cos(\beta)^2 + \cos(\gamma)^2 = 1$  (as constraint). We provide the MATLAB source code (*Fit\_Ellipsoid.m*) that performs the fit to any arbitrary shape. The input is a 3D pixelated matrix ( $D$ )

where 0 is for host and 1 is for inclusion. The matrix  $D$  describes the shape of an arbitrary inclusion shape. The output is the best-fitted effective ellipsoid's axes lengths and orientations. As an example, the fit is performed for an ellipsoid and the result  
710 returns the originally prescribed axes lengths.

### Summary of supplementary files

The supplementary files include codes for calculating: 1) the Eshelby's tensor  $S_{ij}$  and the dimensionless matrix  $M_{ij}$  (in Eq. 8), which are used to calculate the residual stress or strain (*Calculate\_Eshelby.m*); 2) the best-fitted effective ellipsoid's axes  
715 lengths and orientations (*Fit\_Ellipsoid.m*). 3) the strain tensor based on lattice parameters at reference room  $P$ - $T$  conditions and entrapment conditions for any symmetry systems. Details of the codes are given here for users to apply them. The raw data from FE simulation are also provided for reproduction of the figures.

#### 1) Code: *Calculate\_Eshelby.m*

The inputs are listed below (*italic with underline denotes MATLAB variables*):

720  $C_{incl}$ : the inclusion's anisotropic elastic stiffness tensor at room  $P$ - $T$ .

$G_{host}$ : the isotropic host's shear modulus at room  $P$ - $T$ .

$K_{host}$ : the isotropic host's bulk modulus at room  $P$ - $T$ .

$\nu_{host}$ : the isotropic host's Poisson ratio calculated from  $G_{host}$  and  $K_{host}$ .

725  $a$ ,  $b$ ,  $c$ : geometrical principal axes lengths of ellipsoidal inclusion. They are parallel to  $x$ ,  $y$  and  $z$  coordinate axes. Note they are not the lattice parameters.

The outputs are as follows:

$S$ : the Eshelby's tensor  $S_{ij}$

$M$ : dimensionless  $M_{ij}$  matrix that can be plugged into Eq. 8.

#### 2) Code: *Fit\_Ellipsoid.m*

730 The inputs are as follows:

$D$ : 3D pixelated matrix (3D image) describing the shape of the inclusion. The value 1 is given for pixels within the inclusion and 0 is given for pixels outside the inclusion.

$dx$ ,  $dy$ ,  $dz$ : spatial increment of the 3D image, i.e. the size of each 3D cuboidal pixel.

735 An example is given for ellipsoid fitting. The variables  $a$ ,  $b$ ,  $c$  are the axes' lengths of the ellipsoid. After running the code, we obtain the best-fitted axes' lengths which are the same as the input.

The outputs of the code are as follows:

$A$ : axes' lengths of the best fitted inclusion (sorted from maximal to minimal principle axes of the best-fitted effective ellipsoid)

$B$ : directional cosine of the maximal, intermediate and minimal principle axes. Converting directional cosine to angle ( $\alpha$ ,  $\beta$  and  $\gamma$ ) can be easily done by using "acos" function in MATLAB.

740 After running the code, the message "Optimization completed because the objective function is non-decreasing in feasible directions" should be displayed on the command window. This means the run is successful. The best-fitted effective ellipsoid's axes lengths and orientations will also be displayed. As this is a non-linear optimization, local minima may be reach for some special inclusion shape or convergence is not obtained that leads to failure of the run. In this case, the initial guess of the orientation needs to be changed. It may be needed to change " $\chi_0$ " variable in the "Fit\_Ellip.m" function. One may modify the  
745 initial guess " $\chi_0$ " or contact the author at [xinzhong0708@gmail.com](mailto:xinzhong0708@gmail.com) for support.

### 3) Code: *Calculate\_Strain.m*

This code calculates the lattice strain at entrapment condition using lattice parameters at both reference room conditions and entrapment conditions. The inputs are the lattice parameters at room conditions  $a_0$ ,  $b_0$ ,  $c_0$  and  $\alpha_0$ ,  $\beta_0$ ,  $\gamma_0$ , and lattice parameters at entrapment conditions  $a$ ,  $b$ ,  $c$  and  $\alpha$ ,  $\beta$ ,  $\gamma$ . The output are the strain in Cartesian coordinate system. The Cartesian  $x$ -axis is  
750 parallel to crystallographic  $a^*$ -axis and  $z$ -axis parallel to  $c$ -axis by convention. The reported strain tensors include infinitesimal and finite Lagrangian strain, which are close to each other for small strain problems and the difference is well below the detection limit of any analytical techniques.

### 4) Excel raw data for FE model

The file "*FE\_regular.xlsx*" and "*FE\_random.xlsx*" are the calculated raw data for section 4.3 and section 4.4. The data can be  
755 used to reproduce Fig. 6, Fig. 7 and Table 1.

### 5) Animation of random inclusion shape (for section 4.4 "random faceted shape")

The 3D random inclusion shapes are visualized as cartoon in "*Random\_3D\_Shape.gif*" file. It can be viewed by dragging into any IE browser. Details of generating the random inclusion shape with random crystallographic orientation is given in the main text.

760